

Modelling tidal-induced sediment transport in a sand-silt mixed environment from days to years: Application to the Jiangsu coastal water, China

Yao, Peng; Su, Min; Wang, Zhengbing ; van Rijn, L.C.; Zhang, Changkuan; Stive, Marcel

DOI

[10.1016/j.coastaleng.2018.09.002](https://doi.org/10.1016/j.coastaleng.2018.09.002)

Publication date

2018

Document Version

Final published version

Published in

Coastal Engineering

Citation (APA)

Yao, P., Su, M., Wang, Z., van Rijn, L. C., Zhang, C., & Stive, M. (2018). Modelling tidal-induced sediment transport in a sand-silt mixed environment from days to years: Application to the Jiangsu coastal water, China. *Coastal Engineering*, 141, 86-106. <https://doi.org/10.1016/j.coastaleng.2018.09.002>

Important note

To cite this publication, please use the final published version (if applicable).
Please check the document version above.

Copyright

Other than for strictly personal use, it is not permitted to download, forward or distribute the text or part of it, without the consent of the author(s) and/or copyright holder(s), unless the work is under an open content license such as Creative Commons.

Takedown policy

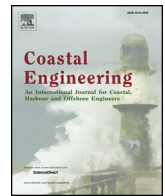
Please contact us and provide details if you believe this document breaches copyrights.
We will remove access to the work immediately and investigate your claim.

Green Open Access added to TU Delft Institutional Repository

'You share, we take care!' – Taverne project

<https://www.openaccess.nl/en/you-share-we-take-care>

Otherwise as indicated in the copyright section: the publisher is the copyright holder of this work and the author uses the Dutch legislation to make this work public.



Modelling tidal-induced sediment transport in a sand-silt mixed environment from days to years: Application to the Jiangsu coastal water, China

Peng Yao^{a,b}, Min Su^{a,b,*}, Zhengbing Wang^{b,d}, Leo C. van Rijn^c, Changkuan Zhang^e, Marcel J.F. Stive^b

^a Institute of Estuarine and Coastal Research, School of Marine Sciences, Sun Yat-Sen University, No. 135, Xingang Xi Road, Guangzhou, 510275, China

^b Faculty of Civil Engineering and Geosciences, Section of Hydraulic Engineering, Delft University of Technology, P.O.Box 5048, 2600 GA, Delft, the Netherlands

^c Leo van Rijn Sediment Consultancy, Domineeswal 6, 8356 DS, Blokzijl, the Netherlands

^d Deltares, P.O.Box 177, 2600 MH Delft, the Netherlands

^e College of Harbor, Coastal and Offshore Engineering, Hohai University, 1 Xikang Road, Nanjing, 210098, China

ARTICLE INFO

Keywords:

Sediment transport
Sand-silt mixed bed
Tide
Short-term and long-term simulation
Jiangsu coast

ABSTRACT

In the present study a new multi-fractional, depth-averaged sediment transport module was developed and embedded into a morphodynamic model for a sand-silt mixed shallow water environment. Subsequently, the model was applied to the case of the Jiangsu coast, which features a silt enriched sedimentary environment bordered by two large-scale geomorphological units: the Old Yellow River Delta (OYRD) in the north and the Radial Sand Ridge Field (RSRF) in the south. Based on this case, the predictive abilities of the present model are assessed on both the short-term and the long-term. Comparisons with measurements over two successive tidal cycles indicate that the present model produces very good results on short-time scales. The model performance is extended and further validated by comparing the overall annual Suspended Sediment Concentration (SSC) pattern, the annual morphological changes, the annual sediment budget and the evolution trend of the bed composition. Also, these long-term results agree well with existing observations over the past several decades. Hence, an essential feature of the present modelling approach is the ability to simulate sediment transport and morphological changes over a relatively long time span (i.e., time scale of years) in a sand-silt mixed sedimentary environment, based on its validated short-term performance.

1. Introduction

Sediment transport plays a significant role in morphological processes over different spatial and temporal scales, especially in shallow coastal waters such as estuaries, tidal inlets and lagoons, open coasts etc. (Dronkers, 1986; Dyer, 1986; Le Hir et al., 2001; Uncles, 2002; Collins and Balson, 2007; Fagherazzi and Overeem, 2007). There are many studies to formulate sediment transport for pure non-cohesive sediments (Nielsen, 1992; Soulsby, 1997; van Rijn, 1993; etc.) and cohesive sediments (see Winterwerp and van Kesteren, 2004 for an overview). In these theories, the non-cohesive sediment is defined as the particle size larger than 62 μm ; while the cohesive sediment refers to grain sizes smaller than 62 μm (also named as mud, i.e., sum of the silt and clay fractions).

Natural bottom sediments in the coastal region are rarely composed

of grains with one size but rather of various sizes. Different sediment fractions behave different resulting in a selective sediment transport (Greenwood and Xu, 2001), especially in case that the bottom sediments are composed of both cohesive and non-cohesive materials. Previous experiments have demonstrated that the critical bed shear stress can increase dramatically with the increase of the clay component in the mixture (Mitchener and Torfs, 1996; Jacobs et al., 2011). In order to predict sediment transport over a mixed sediment bed, several sand-mud modules were developed (Carniello et al., 2012; Le Hir et al., 2011; van Ledden et al., 2006; Waeles et al., 2008). Most sand-mud modules divide the mixed sediment into non-cohesive and cohesive fractions by a particle size of 62 μm and separately resolve the sediment transport equations using non-cohesive sediment and cohesive sediment formulations (e.g., Partheniades-Krone formulations (Partheniades, 1965)). The influence of the cohesive mud fraction is taken into account

* Corresponding author. Institute of Estuarine and Coastal Research, School of Marine Sciences, Sun Yat-Sen University, No. 135, Xingang Xi Road, Guangzhou, 510275, China.

E-mail address: sumin5@mail.sysu.edu.cn (M. Su).

<https://doi.org/10.1016/j.coastaleng.2018.09.002>

Received 2 April 2018; Received in revised form 13 July 2018; Accepted 9 September 2018

Available online 15 September 2018

0378-3839/© 2018 Elsevier B.V. All rights reserved.

by a critical value of mud content. This method has been applied in several estuaries, tidal inlets and lagoons, etc. (Le Hir et al., 2011; van Ledden et al., 2006).

Besides the above mentioned cohesive mud (or clay-dominated mud), there is another type of mud, namely, silt-dominated mud (weakly or non-cohesive) which is abundant in China, for example, at the Jiangsu coast (Wang, 2002). Silt with sizes ranging from 8 μm to 62 μm is mainly composed of quartz and feldspar, which are basically non-cohesive (Lambe and Whitman, 1979; van Rijn, 2006). Several previous wave flume and wave tunnel experiments on silt-enriched sediments (with experimental sediment sizes ranging from 20 μm to 90 μm) have confirmed that the sediment transport processes are different from both the cohesive sediment and non-cohesive sediment, but may hold dual-features (Hooshmand et al., 2015; Lamb and Parsons, 2005; te Slaa et al., 2013; Yao et al., 2015; Zhao, 2003). For example, ripples are observed as bed forms instead of a fluid mud bed, based on the experiments of Lamb and Parsons (2005) on silts with a size of 20 μm under pure wave conditions. The sediment dynamics of silt-enriched bed mixtures are greatly different from the erosion processes of cohesive mud (Yao et al., 2015). By appropriate calibration, the above mentioned sand-mud module, which treat the entire mud content as cohesive, can probably be applied to silt-dominated mud over periods from days to weeks. However, regarding long-term sediment transport (i.e., from months to years), the sand-mud module would not be applicable due to an inappropriate formulation in silt-dominated bed (Mehta and Lee, 1994).

Van Rijn (2007a, b) proposed a unified model framework using a diffusion concept to formulate sediment transport of fine silts to coarse sand and gravel (from 8 μm to 2000 μm ; sediment classification and grain size scale refers to American Geophysical Union). Based on several datasets of flume experiments, Yao et al. (2015) re-calibrated several formulations of van Rijn (2007a, 2007b, hereinafter referred to as vRijn07), and presented a multi-fractional 2DV sediment transport module for sand-silt mixed sediment. Comparisons between predictions and measurements show a good model performance in laboratory with two sand-silt mixed bed settings. Therefore, it is worthwhile to introduce this methodology to study sediment dynamics in different spatial and temporal scales with real cases, such as the Jiangsu coast, China.

The objective of the present research is to study successively modelling sediment transport in a sand-silt mixed environment from the perspective of both short-term and long-term scales. To this end, a new strategy dealing with sand-silt mixtures is proposed and utilized through a morphodynamic model (Delft3D). Subsequently, the model is applied to the inner shelf along the Jiangsu coast, which is characterized by a silt-enriched sedimentary environment. Meanwhile, efforts have been made to reasonably represent the complicated bottom sediment composition in the Jiangsu coastal waters. The model performance regarding the short-term is first assessed by two independent measurements on both hydrodynamics and Suspended Sediment Concentrations (SSCs). The model performance regarding the long-term period is further assessed by previous observation-based understandings in terms of the spatial pattern of SSCs, the annual morphological changes, the annual sediment budget and the evolution trend of bed composition.

2. Method

2.1. Sediment transport model

Our previous experimental results suggest that it is necessary to separately model the transport of silt and sand fractions over a sand-silt mixed bed (Yao et al., 2015). A stand-alone multi-fractional 2DV sediment transport module is developed based on updated vRijn07 formulations to predict the sediment transport. In this study, the previously developed sediment transport module was merged into an open

source modelling system Delft3D. In Delft3D, the flow field is computed by solving the Reynolds-averaged Navier-Stokes equations on a staggered model grid using a finite-difference-scheme (Deltares, 2011; Lesser et al., 2004). Subsequently, the sediment transport is calculated at each half time step by the integrated sediment transport model using the flow results. Besides, the suspended-load transport and bed-load transport are calculated separately. The separation of the transport modes is based on a reference height proposed by van Rijn (1993). Bed level changes are updated at every flow/sediment time step according to the sediment mass balance (see Section 2.2 for detail).

Transport of the suspended load (above reference height) is calculated by solving an advection-diffusion equation. In the present study, a two-Dimensional-Horizontal (2DH; i.e., depth-averaged) mode is applied for the computation of both flow and suspended sediment transport. For the multi-fraction suspended sediment, the depth-averaged advection-diffusion equation is written as:

$$\frac{\partial(h\bar{c}_i)}{\partial t} + \frac{\partial(h\bar{u}\bar{c}_i)}{\partial x} + \frac{\partial(h\bar{v}\bar{c}_i)}{\partial y} = h \left[\frac{\partial}{\partial x} \left(\varepsilon_{s,x,i} \frac{\partial \bar{c}_i}{\partial x} \right) + \frac{\partial}{\partial y} \left(\varepsilon_{s,y,i} \frac{\partial \bar{c}_i}{\partial y} \right) \right] + hS_i, \quad (1)$$

in which, \bar{c} is the depth-averaged suspended sediment concentration; h is the total water depth; u , v are the flow velocities in x , y -directions respectively; $\varepsilon_{s,x}$, $\varepsilon_{s,y}$ are the horizontal sediment diffusion coefficients in x , y -directions respectively; S represents the source and sink terms (i.e., deposition and erosion) per unit area of the bed and S has a form of $S_i = \alpha_{R,i} w_{s,i} (\bar{c}_{e,i} - \bar{c}_i)$ (Falconer and Owens, 1990; Wang, 1992, 1989; Wu, 2004); α_R is the relaxation coefficient, because the suspended sediment concentrations do not respond instantaneously to the flow and it takes time to reach the equilibrium concentration (Wang, 1992; Wang and Ribberink, 1986), and α_R is calculated based on the Galappatti's (1983) method in this study; w_s is the settling velocity of the suspended sediment; \bar{c}_e is the depth-averaged equilibrium concentration; the subscript i represents the corresponding coefficient of the sediment fraction i . The horizontal diffusivity coefficients are taken from the flow module.

Regarding the equilibrium (steady and uniform), the depth-averaged sediment concentration \bar{c}_e and the basic parameters for deriving \bar{c}_e , are based on the updated formulations of vRijn07 in our previous study (Yao et al., 2015). In each hydrodynamic grid, the initial single vertical layer is refined into 20 sub-grid (virtual) points (with a logarithmic distribution of the layer thickness) to calculate the vertical equilibrium concentration profile as well as the depth-averaged equilibrium concentration \bar{c}_e .

The calculation of the bed-load transport is based on a quasi-steady approach. Thus, the bed-load transport is assumed to react instantaneously to flow. In the current-only case, the instantaneous bed-load transport is calculated by van Rijn (2007a):

$$S_b = 0.5 \rho_s p_i D_i f_{silt,i} \left(\frac{\tau'_i}{\rho} \right)^{0.5} \frac{T_i}{D_{*,i}^{0.3}}, \quad (2)$$

where, $f_{silt,i}$ is a silt factor, and $f_{silt,i} = d_{sand}/D_i$ ($f_{silt,i} = 1$ for $D_i > d_{sand} = 62 \mu\text{m}$); D_i is median grain size of fraction i ; p_i is the relative availability of sediment fraction i , and p_i is updated with the changes of the bed composition during simulation; $D_{*,i}$ is the dimensionless particle size, and $D_{*,i} = D_i [(s-1)g/\nu^2]^{1/3}$; ν is the kinematic viscosity; τ'_i is the effective current-related bed shear stress; T_i is the excess bed shear stress (see Appendix B).

By implementing above mentioned updated formulations of sediment transport, individual solvers are used for the calculation of settling velocities, equilibrium concentrations, source-sink terms (i.e., deposition and erosion with consideration of relaxation effect), suspended load and bed-load transport. The considered physical processes are: flocculation effects; hindered settling effects; effects of the cohesion and packing density on the critical bed shear stress; hiding and exposure effects on critical bed shear stress; stratification effects (turbulence damping through eddy viscosity of flow) in case of a high

sediment concentration; bed slope effects on the critical bed shear stress and the bed-load transport. These above mentioned processes are taken into account by both the median grain size of the mixed bed ($D_{50,bed}$) and the grain size of each sediment fraction (D_i). A detailed description for the determination of the relevant parameters is given in the Appendix B.

2.2. Bed level and bed composition update

Bottom changes are calculated based on the mass balance of the sediment:

$$\frac{\partial(1-\eta)z_b}{\partial t} + \frac{\partial(S_{b,x} + S_{s,x})}{\partial x} + \frac{\partial(S_{b,y} + S_{s,y})}{\partial y} = 0, \quad (3)$$

where, $S_{b,x}$ and $S_{b,y}$ are the bed-load transport in x and y directions; $S_{s,x}$ and $S_{s,y}$ are the suspended load transport in x and y directions; η is the porosity of the bed. The sediment grains have a density (ρ_s) of 2650 kg/m³. The dry bulk density of the mixed sediment bed (i.e., including pores) is dependent on the median grain size through (van Rijn, 2007a):

$$\rho_{dry} = \begin{cases} 0.65\rho_s \left(\frac{D_{50,bed}}{d_{sand}} \right), & D_{50,bed} < d_{sand} \\ 0.65\rho_s, & D_{50,bed} \geq d_{sand} \end{cases}, \quad (4)$$

in which, $D_{50,bed}$ is the median grain size of the mixed bed and $D_{50,bed}$ is calculated based on the sediment fractions assuming a piecewise log-uniform distribution within each sediment fraction; $d_{sand} = 62 \mu\text{m}$. The overall available sediment mass of each fraction in the bed is updated simultaneously with the bed level changes. This implies that the porosity of the mixed bed is updated correspondingly.

The bed composition is simulated as a layered stratigraphy system (Hirano, 1971; van der Wegen et al., 2010). Only the topmost layer of the bed (i.e., the transport layer) is active and interacting with the water column by means of erosion and sedimentation. The transport layer has a fixed thickness during the whole simulation period. In case of erosion, the thickness of the transport layer can be replenished from the layer below (i.e., sub-layers). In case of deposition, the new deposits first mix with sediments in the transport layer, and subsequently merge with the sub-layers to keep the thickness of the transport layer unchanged. Hence, the bed composition of the layered system is updated. The median grain size of the mixed bed in the topmost sediment layer is changed correspondingly, which would result in changes of the critical bed shear stress for the initiation of sediment motion, and consequently the determination of the equilibrium concentration.

3. Application to the Jiangsu coastal waters

3.1. General information of the Jiangsu coast

The Jiangsu coast is located in eastern China, facing the South Yellow Sea. The coastline of Jiangsu, starting from the Xiuzhen River Estuary in the north, extends southward to the Yangtze River Estuary, with a total length of ~954 km. The silty coast dominates ~93% of the total shoreline (Ren, 1986). A large-scale and well-developed tidal flat system is mainly located along the central part of Jiangsu coast, sheltered behind the sand ridge system (i.e., the Radial Sand Ridge Field). The width of the tidal flats is about 10–13 km and the maximum width can reach up to 36 km (Wang and Zhu, 1990). In this study, the inner shelf is defined as the region starting at the Jiangsu coastline toward a depth of around 50 m (i.e., approximately the western edge of central Yellow Sea trough; see Fig. 1). The average water depth of this region is around 30 m with a gentle bottom sloping toward the sea. Based on features of hydrodynamics, sediment properties as well as morphodynamics, the whole Jiangsu coast can be divided into three sub-geomorphological units (Fig. 1a): the Haizhou Bay, the Old Yellow River Delta (OYRD) and the fan-shaped Radial Sand Ridge Field (RSRF).

The RSRF is located in the central and southern Jiangsu coast and made up by 70 sand ridges of various sizes radiating from Jianggang town (Fig. 1). The ridge-channel system in the RSRF totally covers an area of ~22470 km² (Ren, 1986). There are 9 major ridges, which can emerge during low tidal waters, with area of individual ridge ranging from 23 km² to 780 km² (Wang, 2014; see Fig. 1c). The paleo-Yangtze River derived sands are considered to provide fine sand substrate (thickness > 10 m) for the RSRF. The morphology of the RSRF is quite unique in both shape and size compared with their linear counterparts (as shown in Dyer and Huntley, 1999). The OYRD was developed during 1128–1855 AD, when the Yellow River discharged into the South Yellow Sea via the northern Jiangsu coast. During that period, the Yellow River brought considerable amounts of fine silts to the Jiangsu coast, continuously prograding the shoreline seaward, forming not only the OYRD but also a large-scale tidal flat system in the central Jiangsu coast (Gao, 2009; see Fig. 1b) and rapid growth of the RSRF (Su et al., 2017a). After 1855, the lower Yellow River shifted northward, discharging into the Bohai Sea. Consequently, the OYRD (both subaerial and submarine delta area) was subject to severe erosion. In contrast, tidal flats and the RSRF are still dominant by accretion (Su et al., 2017b). Thus, morphological changes along the Jiangsu coast can be roughly described as: an erosion-dominant open coast in the north and an accretion-dominant ridge-sheltered coast in the south (Ren, 1986; Liu et al., 2011).

The Jiangsu coast is subject to a subtropical monsoon climate, and the seasonal sea surface temperature varies from 5.6 to 31.0 °C (Zhang, 2012). There are several small rivers discharging into the sea along the Jiangsu coast. Most of the rivers are channelized and have small discharges. The Yangtze River discharges into the sea in the southernmost of the study area. Approximately 10% of the total discharge from the Yangtze River may flow northward, diluting the salinity in the near-Estuary region (i.e., southernmost of the RSRF). The seasonal variation of the salinity in this area is relatively small with the annual-averaged salinity of 29.5‰–32.2‰. Both sea water temperature and salinity are homogeneous over the water depth (i.e., well-mixed) in most areas along the Jiangsu coast (Wang, 2002).

The tide, especially the semi-diurnal tide, is the dominant forcing in the Yellow Sea (Choi, 1984; Fang, 1986; Su et al., 2015). The mean tidal range along the coast is between 2 and 4 m. The mean tidal flow velocity is weak in the Haizhou Bay (between 0.3 and 0.5 m/s) and in the OYRD (between 0.6 and 1.0 m/s), but it becomes stronger in the RSRF. The tidal flow velocity can be larger than 2 m/s in several major tidal channels of the RSRF during spring tide. The wind is predominantly from the NE or ENE in winter and from the SE or ESE-SSE in summer. Statistically, the NE wind is stronger than the SE wind. The mean wind speed over the sea surface is between 5 and 7 m/s. The waves are mainly controlled by monsoon climates varying both spatially and temporally. In the whole region, the significant wave heights are smaller than 1 m (He et al., 2010).

Influenced by the huge Yellow River derived sediments, the fine-grained sediment is dominant on the floor of the inner shelf along the Jiangsu coast, with a pronounced silt content (Alexander et al., 1991; Lee and Chough, 1989; Ren and Shi, 1986). On the other hand, spatial distributions of the surface bed sediment types (e.g., classified based on Shepard (1954) method) in the study area are rather complex due to the complex sediment sources in different historical periods, the energetic hydrodynamic conditions and the complex bathymetries along the coast (Liu et al., 1989; Wang and Ke, 1997; Y. Wang et al., 2012; Zhang, 2012). In the Haizhou Bay, the sediment is mainly composed of fine sand (> 125 μm). In the OYRD and in the tidal channels of the RSRF, the contents of fine silt and clay (< 30 μm) increase, and the main sediment type is clayey/fine silt (8–30 μm). On the ridges of the RSRF, the contents of coarse silt and fine sand (> 30 μm) increase, and the main types of sediment are sandy silt and silty sand (30–125 μm). In the offshore area where the depth is more than 30 m, the sediment becomes finer seaward as sand, sandy silt and clayey silt, respectively. Overall,

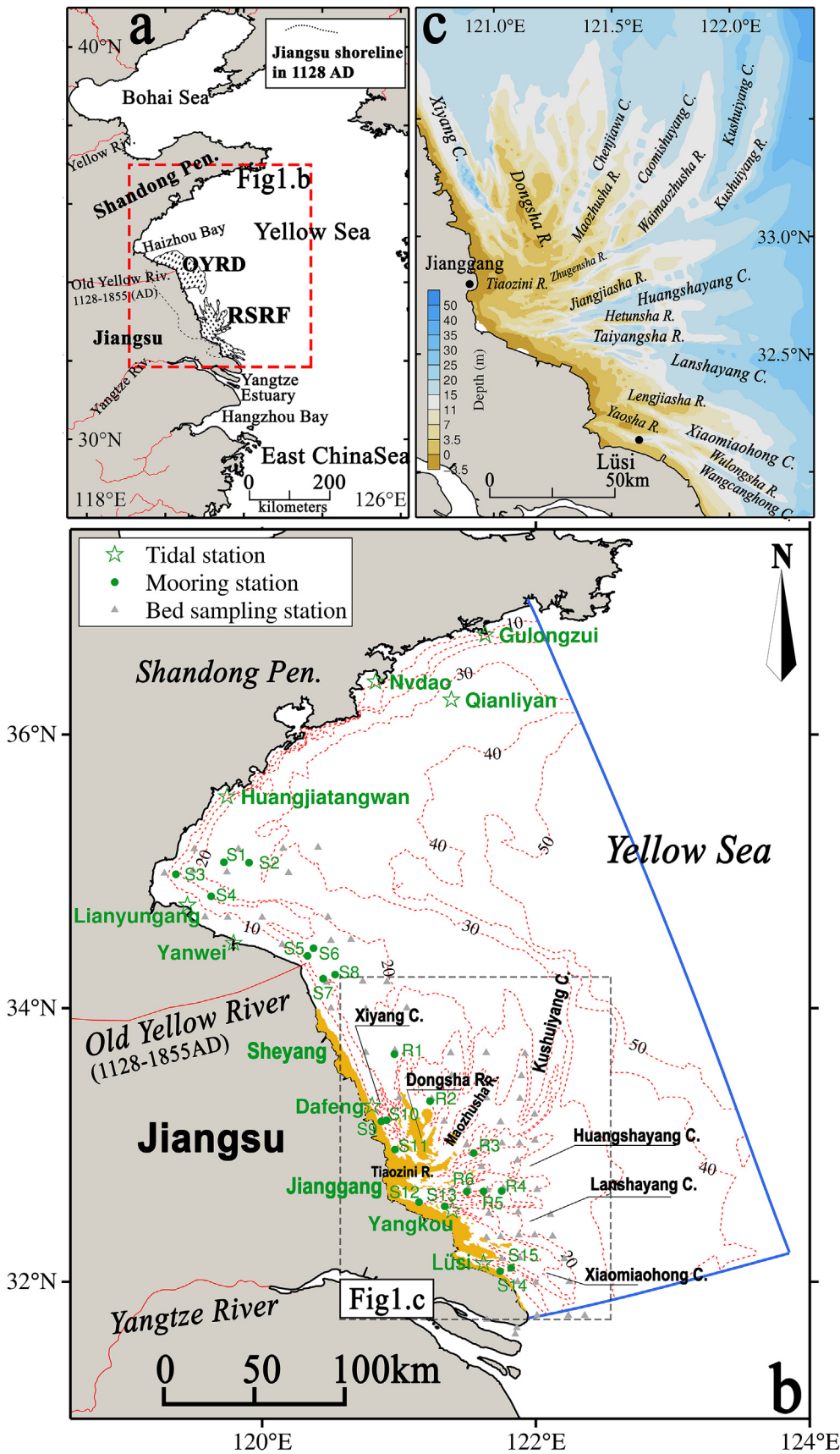


Fig. 1. Regional setting of the study area. (a) Location of the inner shelf along the Jiangsu coast, China (see the red rectangle). The shaded areas roughly denote the location of the OYRD and RSRF. OYRD = Old Yellow River Delta; RSRF = Radial Sand Ridge Field. (b) Bathymetry map and observation stations in the Jiangsu coastal zone. The yellow coloured patches denote the shallow water zones (i.e., tidal flats and ridges), which can emerge during low tide. (c) Enlarged area of the RSRF. For clarity, the names of the ridges and tidal channels are labelled in the corresponding positions in the figure. (For interpretation of the references to colour in this figure legend, the reader is referred to the Web version of this article.)

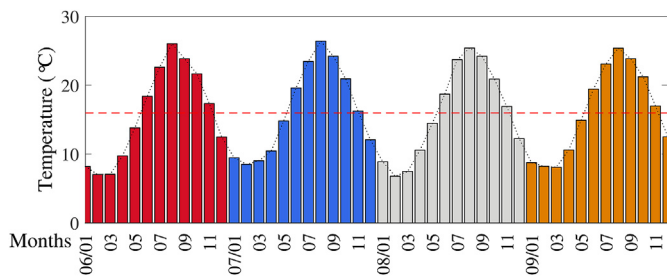


Fig. 2. The regional-averaged monthly-mean SST in the Jiangsu coastal waters during 2006–2009. Red dashed line denotes averaged SST during 2006–2009 ($\sim 16^\circ\text{C}$). (For interpretation of the references to colour in this figure legend, the reader is referred to the Web version of this article.)

the grain sizes of the bottom sediment grains nowadays range from 8 to $250\ \mu\text{m}$ with pronounced silt contents.

3.2. Configurations of the Jiangsu Regional Model (JRM)

The aforementioned modelling framework (i.e., standard Delft3D integrated with the updated sediment transport module) is utilized to setup the Jiangsu Regional Model (JRM). The computational model domain of the JRM almost covers the whole inner shelf along the Jiangsu coast, bounded by the latitudes 32° and 36.5° and by the longitudes 119° and 124° (i.e., $\sim 200\ \text{km} \times \sim 550\ \text{km}$, see Fig. 1b). Given such a large-scale domain, the boundary fitted orthogonal curvilinear grid is applied with a grid size varying from $0.42'$ nearshore to $0.71'$ offshore (i.e., $608\text{--}1216\ \text{m}$) under spherical coordinates. Under this configuration, we mainly focus on modelling sediment transport over large-scale channel-shoal system while neglecting small-scale secondary channels migration. van der Wegen et al. (2008) suggested that small-scale patterns do not impact the major morphodynamic features and the influence of grid size reduces especially in open coastal area. Hence, the present grid ($600\text{--}700\ \text{m}$ nearshore) is sufficient to solve major pattern characteristics. The present model can further be nested with fine resolution local-scale models (e.g. tidal flat) to examine sediment transport in more detail, but this is considered outside the scope of this study.

As mentioned earlier, tide is the dominant forcing in the Yellow Sea, whereas the wind and wave forces are considered of secondary importance and mainly play a role in local hydrodynamics (Xing et al., 2012) and local morphological changes (Zhang et al., 1999). Since our primary objective is to assess the ability of the present modelling framework in a mixed sand-silt environment, we only focused on the dominant driving force (tide), i.e., the first-order assessment. The secondary effects of wind and wave, which require more detailed study with enough data, are not explored here.

Two open boundaries are set at the easternmost and southernmost of the domain, respectively. 13 tidal harmonic components (i.e., M2, S2, K2, N2, K1, O1, P1, Q1, M4, MS4, MN4, MF, MM), which were initially derived from the one-year time-series water level results (with 10 min output intervals) of a large-scale tidal wave model (Su et al., 2015), are used to drive the astronomical tides at the open boundaries of the JRM. Note, the one-year run of the large-scale tidal wave model includes the discharge of the Yangtze River with a multi-year averaged value of $29500\ \text{m}^3/\text{s}$ (Guo et al., 2015).

The initial bathymetry data (Fig. 1b) was built up based on (1) the measurements in 2006 in the RSRF (Zhang, 2012); (2) the nautical charts published by the Navigation Guarantee Department of the Chinese Navy Headquarters. As mentioned in Section 3.1, the river discharges are rather small along the Jiangsu coast. Therefore, the river discharge is expected to have little influence on the flow regimes in this region and is not included here. It is suggested that the influence of the Yangtze River on the tidal regimes is localized in the near-field of the

estuary (not further north than 32°) (Su et al., 2015). Nevertheless, the influence of the Yangtze River is still considered when generating open boundary conditions by the large-scale of the tidal wave model. Bottom friction is prescribed by a Manning coefficient, which is treated as a tuning parameter during calibration (see Section 4.1 for more details). Secondary flow is considered in the model because of the complex ridge-channel bathymetry.

Tidal flats and shallow sand ridges periodically become dry and wet during tidal cycles. Therefore, drying and flooding processes are considered in the model. The main scheme is to conduct a series of checks between the total water depth and a pre-defined threshold value ($0.05\ \text{m}$ in this study) on both cell centres (water level point) or cell edges (velocity points, due to staggered grids used) before computation at every half time step. In particular, the water level at the cell edges (velocity points) is calculated by a so-called upwind approach. More details on the drying and wetting scheme see Deltares (2011).

Water temperature and salinity can alter the water properties (e.g., density, kinetic viscosity) and may further influence both the flow velocity and sediment transport. Previous studies suggested that the water temperature is an important factor of influence on seasonal sediment dynamics (Krögel and Flemming, 1998). Since the sea water temperature and salinity are basically homogeneous over the depth (i.e., well-mixed) in the study area (Wang, 2002), the monthly mean Sea Surface Temperature (SST) is used in this study as a time-varying but spatial-constant coefficient. The SSTs in the study area are obtained from the COBE SST data provided by the NOAA/OAR/ESRL PSD (<http://www.esrl.noaa.gov/psd/>). Fig. 2 shows the regional-averaged monthly-mean SST during 2006–2009. For salinity of the seawater, a constant value (i.e., 30‰) is set in the model, as it exhibits less variation throughout the year. Preliminary model sensitivity tests suggest that a time step of 2 min can ensure model stability. In addition to the run with varying temperature (i.e., reference case), we further designed a case with a constant water temperature (hereafter referred to CaseCT) keeping other configurations unchanged. The constant temperature is set to 16°C , which is the averaged temperature during simulation period. Impacts of temperature on sediment dynamics will be discussed in Section 6.2.

3.3. Initial bed composition

As mentioned earlier, the bed sediment types in the inner shelf of the Jiangsu coast vary from fine silt to fine sand and simulating the sediment dynamics over such mixed bed requires a multi-fraction sediment transport model. On the one hand, the implementation of the multi-fraction sediment transport model requires specifying a certain number of sediment fractions, which depend on local conditions (i.e., available measurements). On the other hand, increasing sediment fractions can multiply the computational time. Therefore, it is suggested to include a limited number of sediment fractions (van der Wegen et al., 2010). In the present study, four sediment sizes, viz. fine silt (i.e., $16\ \mu\text{m}$), silt (i.e., $45\ \mu\text{m}$), very fine sand (i.e., $90\ \mu\text{m}$) and fine sand (i.e., $180\ \mu\text{m}$), are selected based on the surface bed sample measurements in 2006 along the Jiangsu coast (see Fig. 1b for sampling stations), on earlier literature (Alexander et al., 1991; Shi et al., 2012; Wang and Ke, 1997) and on a series of preliminary sensitivity runs (not shown here).

Another difficulty, when applying a multi-fraction sediment model, is an appropriate representation of the initial distribution (spatially varying) of the bed composition in the domain, because the available field data on surface bed composition are scarce in most cases. Moreover, the knowledge on the bed composition is crucial for correctly estimating the sediment transport and the corresponding bed level changes (Carniello et al., 2012). Previous studies suggested several alternative approaches for reconstructing the relevant initial distribution of the bed composition: (1) empirically relate the sediment composition with water depth (Amoudry et al., 2014; Blaas et al., 2007); (2) derive

the empirical relationship between the median grain size, and both the local water depth and the horizontal position (Carniello et al., 2014, 2012); (3) reconstruct the sediment composition by using a morpho-dynamic model (van der Wegen et al., 2010). These approaches have been implemented in the bays or lagoons (geophysical length scale of several kilometres), whereas the present study area covers an area of several latitudes and longitudes (i.e., several hundreds of kilometres) with a complex bathymetry and with strong spatial variations of sediment types. Thus, whether these approaches are applicable in this study is unclear.

In this study, we proposed a conceptual approach to reconstruct the distribution of the bed composition as follows. First, the spatial distribution of the bottom sediment types (e.g., clayey silt, silt and silty sand as classified according to the method of Shepard (1954)) is recompiled in the study area, based on the collected surface bed sediment samples in 2006 (see Fig. 1b for sampling stations) and several published studies (Alexander et al., 1991; Wang and Ke, 1997; Shi et al., 2012). Next, the corresponding sediment types are translated into different compositions of sediment fractions. For example, the sediment type of clayey silt is decomposed into 70% of the 16- μm -fraction, 25% of the 45- μm -fraction and 5% of the 90- μm -fraction. Finally, a preliminary simulation was carried out under tidal force using these pre-defined sediment compositions as initial condition. This is to make a first match between hydrodynamics and pre-defined sediment compositions following the methods of van der Wegen et al. (2010) and Luan et al. (2017). The simulation lasts for one month with a layered bed described below. The generated initial spatial distributions of different sediment fractions illustrated coherent channel-ridge variations (Fig. 3). Thus, although the distribution and the content of each fraction are determined arbitrarily, the configuration is (at least qualitatively) consistent with the present understanding of sediment heterogeneity throughout the Jiangsu coastal region.

With respect to the settings of the layered bed stratigraphy, we assume that the initial bed composition is vertically homogeneous with a thickness of 6 m, composed by a transport layer (with a thickness of 0.25 m), ten under-layers (with a thickness of 0.5 m for each layer) and a base layer. Preliminary model tests (not shown here) showed that the entire thickness of the sediment bed is sufficient for the continuous erosion during the modelling period (i.e., three year). Furthermore, in the OYRD where the erosion has been evident since 1855 AD, the initial availability of fine silt (i.e., 16- μm fraction) in the present model, i.e., $1 \times 10^{10} \text{ m}^3$, is comparable to that prescribed by Su et al. (2017a), i.e., $\sim 0.6 \times 10^{10} \text{ m}^3$. Thus, both the spatial sediment composition and the thickness of the erodible sediment are reasonably represented in the model.

3.4. Open boundary conditions for sediment

At the easternmost open boundary, we assume that sediment fluxes, entering the domain through the easternmost boundary, are rather small. The inflow sediment concentration of a 16- μm fraction is set to 0.5 mg/l, keeping the other fractions zero. On the other hand, it is difficult to assign the SSC open boundary condition at the southernmost boundary, because the sediment exchange between the southern RSRF and the Yangtze River is at present still unclear (Wang et al., 2015). For example, Wang (2002) and Wan et al. (2005) reported that approximately 35 million tons of sediments can be transported into the Southern Jiangsu coast each year, accounting for $\sim 9\%$ of the total sediment discharge of the Yangtze River. However, R. Wang et al. (2012) showed that the Yangtze-originated sediment is only activated in the area further south than the Lüsi (latitude of $\sim 32^\circ$; see Fig. 1). Therefore, we collected and surveyed supplementary available field data (e.g., Xing et al., 2010) to determine the southernmost SSC open boundary conditions. We assume that the suspended loads only enter the study area through the shallow waters with depths smaller than 30 m. Subsequently, at the southernmost open boundary segments,

where the depth is smaller than 30 m, the inflow sediment concentration is set to 100 mg/l for a 16 μm fraction (representative SSC fraction from modern Yangtze River; e.g., Saito et al., 2001; Wang, 2002), while keeping the other fractions as zero. Sensitivity simulations with different inflow concentration levels (i.e., 1, 10, 100 and 300 mg/l) are designed and the results will be discussed in Section 6.1.

At open boundaries both the bed level and bed composition are fixed during the simulation. The initial water level, the flow velocity and the suspended sediment concentration are set to zero (i.e., ‘cold start’). Preliminary tests show that 15 days of the simulation is sufficient for the model to spin up. Hence, the first 15 days of simulation are considered as the spin-up period in all simulations.

3.5. Model skill assessment

Model performance can be evaluated quantitatively by a statistical analysis for the agreement between model results and measurements. Fitzpatrick (2009) suggested that a single statistical metric score is insufficient to assess the model skill. Allen et al. (2007) found that the combination of the Nash Model of Efficiency (ME) and Percentage Bias (PB) is sufficiently informative to evaluate an ecological model. van Rijn et al. (2003) and Sutherland et al. (2004) recommended that a measurement error should be taken into account when evaluating a model skill. In this study, the Nash Model of Efficiency (ME) and the Percentage Model Bias (PB) are applied to evaluate the model skill with a consideration of the measurement errors. Following van Rijn et al. (2003), when considering the measurement errors, Nash Model Efficiency (ME) is defined as:

$$ME = 1 - \frac{\sum (|m - p| - \Delta m)^2}{\sum (m - \bar{m})^2}, \quad (5)$$

where, m are the measurements; p are the predictions by the model; \bar{m} is the mean of the measurements, Δm is the error of the measurement and $|m - p| - \Delta m$ should be zero, if < 0 (means no error). Allen et al. (2007) classified four categories to assess the model performance, defined as follows: excellent ($ME > 0.65$), very good ($0.5 < ME < 0.65$), good ($0.2 < ME < 0.5$) and poor ($ME < 0.2$).

The percentage of Bias (PB) considering the measurement error is defined as:

$$PB = \frac{\sum [(m - p) \pm \Delta m]}{\sum m} \times 100\%. \quad (6)$$

At a specific point in the comparison, if $(m - p) > 0$, the numerator of Eq. (6) becomes $(m - p) - \Delta m$. If $(m - p) < 0$, it changes to $(m - p) + \Delta m$ and $(m - p) \pm \Delta m = 0$ if < 0 . The performance levels (using the absolute value of PB, i.e., $|PB|$) are categorized as follows (Allen et al., 2007): excellent ($|PB| < 10\%$), very good ($10\% < |PB| < 20\%$), good ($20\% < |PB| < 40\%$) and poor ($|PB| > 40\%$).

Regarding the field survey carried out in 2006 (Zhang, 2012), measurement errors of the water level and the flow velocity are relatively small, whereas accurate measurement of SSC is still a challenging problem at present. The inaccuracy of the traditional sampling method for SSC measurement is approximately 30% (van Rijn et al., 2000). Therefore, measurement error is set to zero for calculation of model skill scores on water level and flow velocity, while the value of 30% is used as the SSC measurement error.

4. Model calibration and validation on short-term scales (days to months)

4.1. Model calibration on hydrodynamics

The Jiangsu Regional Model was first run with flow only (without computations of sediment transport and morphological changes). The

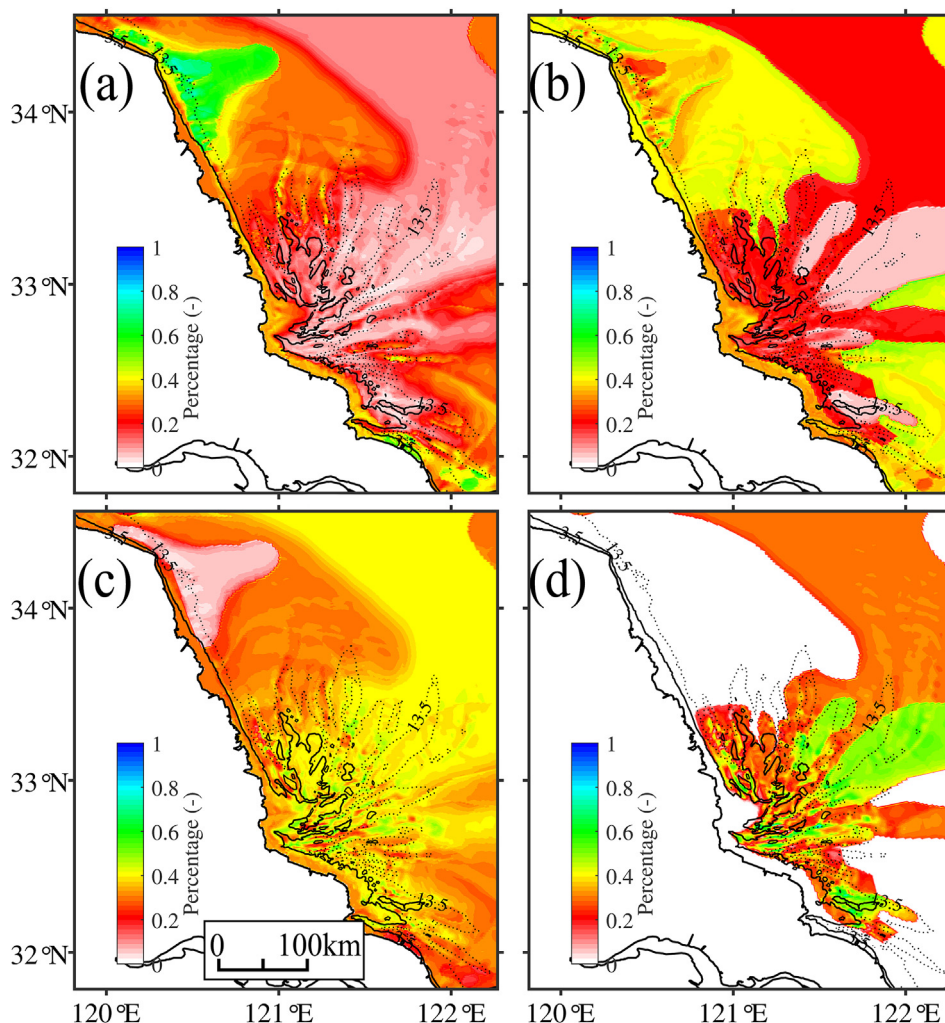


Fig. 3. Initial composition of sediment bed in the inner shelf along the Jiangsu coast with four sediment fractions (by mass). The colours denote the presence of the given sediment classes in the bed. (a) 16 μm fraction; (b) 45 μm fraction; (c) 90 μm fraction; (d) 180 μm fraction. (For interpretation of the references to colour in this figure legend, the reader is referred to the Web version of this article.)

simulation period was from August 1st to September 11th, 2006, covering the relevant measuring period (reported in Zhang, 2012). The roughness coefficient (in this case the Manning coefficient) was applied as a tuning factor for calibration. Due to the complex bathymetry, the Manning coefficient was initially estimated by $n = 0.015 + 0.1/H$ (Xing et al., 2012), where, H is the initial water depth. According to previous studies, depth-averaged SSCs remain high throughout the year (larger than 0.2 g/l, and can reach up to 1.2 g/l) in the coastal area between the OYRD and the central RSRF (Milliman et al., 1986; Wang, 2002; Xing et al., 2010; Zhang, 2012). In turn, the high sediment concentrations can reduce the hydraulic drag as suggested by Winterwerp et al. (2009). Therefore, the Manning coefficient in these corresponding areas was set to a constant value in the model. The computations were compared with the measurements of water levels and flow velocities at 21 mooring stations carried out in August and September 2006 (see Fig. 1b for stations). The optimum setting of the roughness coefficient appeared to be 0.015 in the coastal area between the OYRD and the central RSRF (see model performance in Figs. 4 and 5).

Fig. 4 shows the time-series comparisons between model results and measurements of water level and flow velocity at five stations. These five stations represent the area of the Haizhou Bay (S1), the OYRD (S8), the RSRF (S12, R1 and R5), respectively. Visual comparisons present that both modelled water level and flow velocity agree well with measurements. In addition to visual comparisons, model skills are

evaluated quantitatively by two statistic parameters (i.e., ME and $|PB|$) for all mooring stations (Fig. 5). For the water level, the average ME and $|PB|$ scores over all stations are 0.87 and 12.4% respectively, exhibiting a quasi-excellent model skill. For the flow velocity magnitude, the ME scores at 9 stations are not in the category of excellent (i.e., $ME < 0.65$), and the ME scores show poor skills (< 0.2) at stations S15 and R3. However, the $|PB|$ scores at 18 stations locate in a category of excellent ($|PB| < 10\%$) except stations S10, S14 and S15. Combining the ME and $|PB|$ scores, the simulated flow velocity magnitude has relatively good agreement in most of the stations, at least in the tendency and magnitude (as the $|PB|$ scores shown). The low ME scores at some stations may be due to the inaccurate bathymetric data (e.g., in the area of S15 and R3, where the depth is read from nautical charts with low spatial resolution), and probably due to the complex vertical turbulence structure. In contrast to the flow velocity magnitude, the model shows an excellent skill on estimating the flow velocity direction shown by ME and $|PB|$ scores. It implies that the model has the ability to simulate the flow vector in more accurate manner.

4.2. Model calibration on sediment dynamics and sensitivity analysis

Subsequently, sediment transport and morphological changes were activated and simulated based on hydrodynamics. Simulation periods were same as the flow-only model. The schematization of sediment

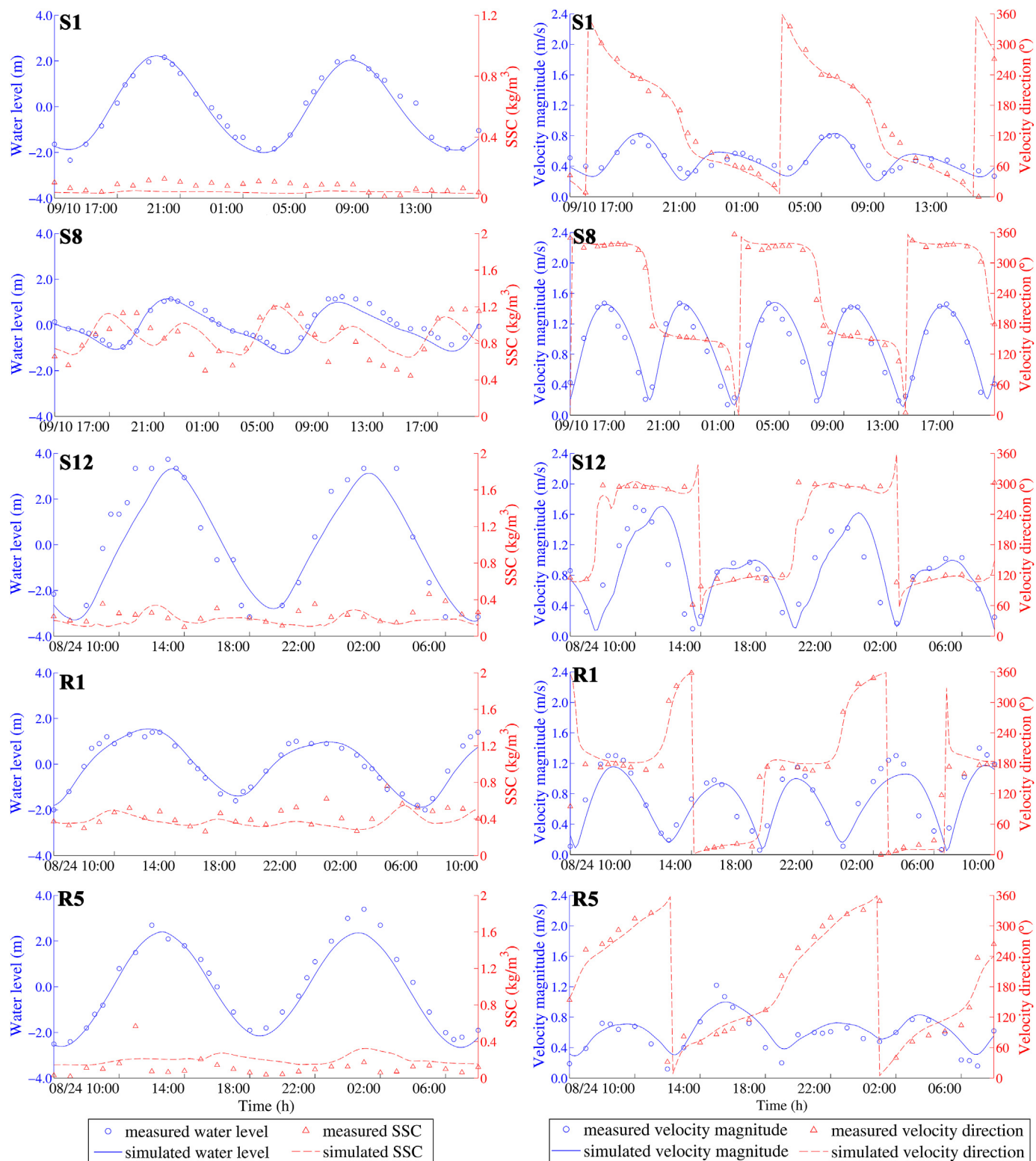


Fig. 4. Comparisons (calibration) between simulated (solid lines) and measured (markers) water levels, depth-averaged velocities (magnitude and direction) and depth-averaged SSCs at five selected mooring stations. Note the measuring period in the Haizhou Bay and OYRD (e.g., station S1 and S8) were from 10th to 11th September 2006, while in the RSRF (e.g., station S12, R1 and R5) were from 24th to 25th August 2006.

fractions for multi-fraction approach and the initial bed composition have been described in detail in Section 3.3. We have designed series of numerical cases in order to examine effects of different physical processes relating to sediment dynamics on performance of the newly integrated sediment transport model. Effects of flocculation, hindered

settling and stratification are explored by numerical cases shown in Table 1. Numerical cases were based on a reference run (considers all processes), deactivating one process while holding the other unchanged. Parameters in sediment transport formulations are applied as default values; see Appendix B for more details. The computations of all

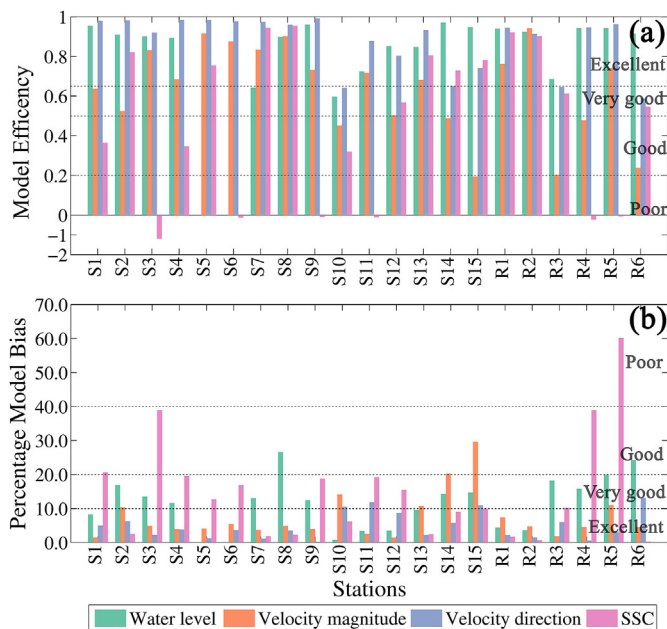


Fig. 5. Summary of the model skills for all the mooring stations (calibration): (a) Nash Model of Efficiency (*ME*) and (b) Percentage of Bias (using the absolute value, i.e., $|PB|$). Note that different colours represent different data (i.e., water level, velocity and SSC). (For interpretation of the references to colour in this figure legend, the reader is referred to the Web version of this article.)

Table 1
Overview of numerical sensitivity cases.

CaseID	Flocculation	Hindered Settling	Stratification
RF	✓	✓	✓
FL	✗	✓	✓
HS	✓	✗	✓
ST	✓	✓	✗

Note: “✓” means that process has been considered in the case; “✗” means that process has been ignored in the case.

cases were compared with the measured SSCs at the same mooring stations as the flow-only model.

Performance of the reference run is shown in Figs. 4 and 5, respectively. Visual comparison illustrated that although agreements between simulations and measurements are not as good as the hydrodynamic results, the magnitude and the overall tendency of the simulation results are still consistent with the measurements. The statistical analyses show that the average *ME* and $|PB|$ of all stations are 0.4 (good skill) and 14.7% (very good skill). Combining the *ME* and $|PB|$ scores, the simulated SSCs do not match the measurements perfectly. However, the $|PB|$ score indicates that, at least, the overall tendency (i.e., the mean base level) of the SSCs is captured by the model.

To compare results of sensitivity cases, results at different stations are categorized into three sub-regions and then region-averaged statistics on *ME* and $|PB|$ are calculated in Table 2. If not considering effects of flocculation, model is failed to reproduce SSCs in the OYRD since both *ME* and $|PB|$ are far away from normal range. This implies a significant role of flocculation processes in the OYRD. Model statistics of caseHS appears similar to reference run, indicating the hindered settling is less important for SSC prediction. When stratification effects are excluded, both *ME* and $|PB|$ become worse throughout the whole domain.

In summary, SSCs in different region are dominant by different processes. Hence, it is recommended to consider all processes relating to sediment dynamics in the Jiangsu coast due to its complex

Table 2
Statistical results of sensitivity runs.

Case	Model Efficiency (–)			Percentage Bias (%)			
	Haizhou Bay	OYRD	RSRF	Case	Haizhou Bay	OYRD	RSRF
	S1-S4	S5-S8	S9-S15 R1-R6		S1-S4	S5-S8	S9-S15 R1-R6
RF	0.08	0.63	0.44	RF	20.41	8.44	14.86
FL	0.08	–51.06	0.11	FL	20.43	181.35	21.42
HS	0.09	0.68	0.44	HS	20.38	7.89	14.85
ST	–2.66	–12.63	–1.95	ST	45.87	76.01	44.17

Note: RF: reference case; FL: case without flocculation; HS: case without hindered settling; ST: case without stratification.

sedimentary environment. The calibration results on sediment dynamics suggest that the overall trend and magnitude of SSCs can be captured by the model despite of not a perfectly match. Therefore, it is concluded that the model shows a reasonable skill for the estimation of SSCs.

4.3. Model verification

After calibration, the model was re-run starting on May 17th, 2006 to June 1st, 2009. The first 15 days are considered as a spin-up period due to zero initial conditions (‘cold start’). Hence, the ‘actual’ simulation period was from June 1st, 2006 to June 1st, 2009, around three years, with a half-hourly output interval for all grid cells. In specific observing stations (see Fig. 1b), the output interval is set to 10 min. The monthly-mean SST used in the model during the simulation period is shown in Fig. 2. There are several field measurements during December 2006 and January 2007 at approximately the same stations as the calibration (Zhang, 2012). These field data are collected to further verify the model performance after half-year simulation.

Figs. 6 and 7 present the model performance in terms of visual comparisons as well as statistical metrics. Herein, we only list model performance on SSCs while verification results on hydrodynamics are illustrated in Supplementary Material. The SSCs at the five stations are underestimated by the model, compared with the measured data (Fig. 6). The *ME* scores at about half of the mooring stations (i.e., 11 stations) are negative, indicating a poor model skill. However, the $|PB|$ scores only show poor skills in the Haizhou Bay, where the flow velocity magnitudes are not well simulated in winter. At other stations, the $|PB|$ scores are smaller than 40%, implying that the base level of modelled SSCs is still close to that of the measurements. On the other hand, the low values of *ME* may be due to (1) the layered bed stratigraphy applied in the model, which can reduce the erosion of the sediment, probably leading to an underestimation in the long term simulation (van der Wegen et al., 2010); (2) the increased critical bed shear stress in winter (due to the low temperatures); (3) exclusion of waves and winds in the present model, which are stronger in winter than in summer.

Furthermore, we designed a case with the same aforementioned simulation period to model sediment transport by traditional method (caseTR). CaseTR treats sediment grains smaller than 62 μm as cohesive sediment by using the Partheniades-Krone formulations, while sediment particle larger than 62 μm are modelled with non-cohesive sediment formulations (herein we use van Rijn, 1993). In caseTR, we only alter the method of calculation sediment transport while keeping other parameters unchanged. More details refer to technical manual of Delft3D (Deltares, 2011). Table 3 shows region-averaged statistics of *ME* and $|PB|$ against measurements for both methods (i.e., caseRF and caseTR). In summer (about two months after simulation starts), caseTR shows good skill on simulating SSCs in the RSRF (*ME* is 0.37), whereas *ME* is rather low in the OYRD and in the Haizhou Bay. The $|PB|$ scores of caseTR are as twice as caseRF but still in a category of good skill. Overall, both methods can simulate acceptable results in a simulation

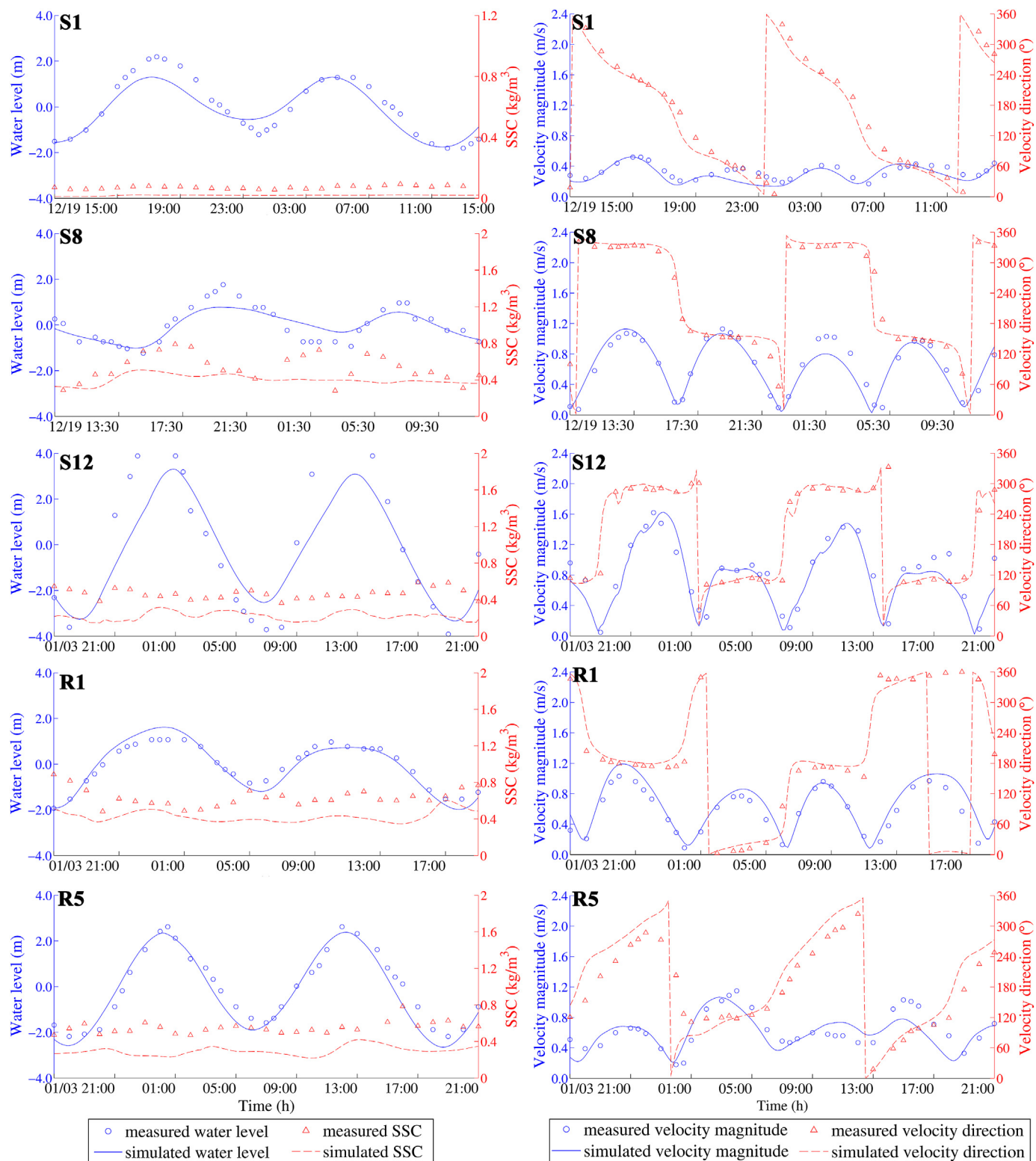


Fig. 6. Comparisons (verification) between simulated (solid lines) and measured (markers) water levels, depth-averaged velocities (magnitude and direction) and depth-averaged SSCs at five selected mooring stations after half-year simulation. Note the measuring period in the Haizhou Bay and OYRD (e.g., station S1 and S8) were from 19th to 20th December 2006, while in the RSRF (e.g., station S12, R1 and R5) were from 3rd to 4th January 2007.

period of two months. After successive simulation period of half year, performances of two cases become relatively poor due to the growth of deviations. CaseTR produces much worse *ME* scores and fails in base level simulations ($|PB| > 40\%$). However, caseRF still produces reasonable base level simulation of SSCs since the $|PB|$ scores are smaller

than 40% in most regions. Comparisons between two simulation methods indicate that with the increase of simulation period, the newly proposed method performs better than the traditional way. Thus, the newly proposed method behaves more robust for successive simulation over days to months.

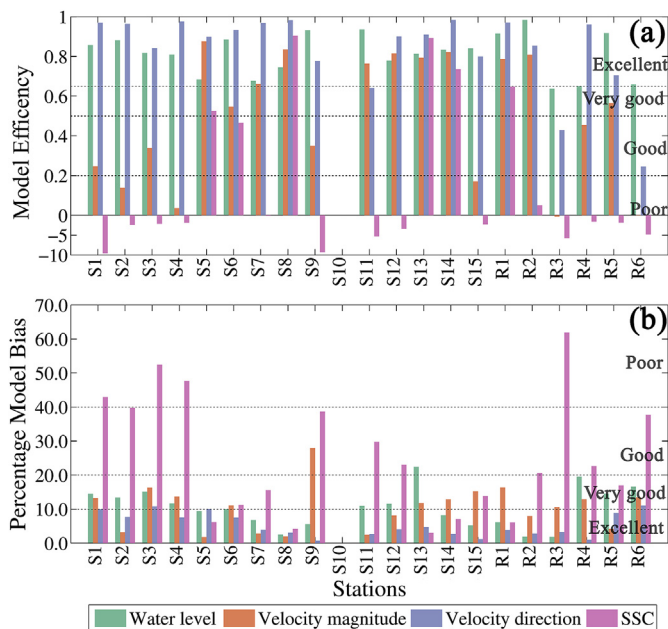


Fig. 7. Summary of the model skills for all the mooring stations after half-year simulation (verification): (a) Nash Model of Efficiency (*ME*) and (b) Percentage of Bias (using the absolute value, i.e., $|PB|$). Note that different colours represent different data (i.e., water level, velocity and SSC). (For interpretation of the references to colour in this figure legend, the reader is referred to the Web version of this article.)

In summary, simulation results of the newly proposed model are in reasonable agreement with the observed data. The model is, therefore, considered validated concerning its ability on consistent simulations of both hydrodynamics and sediment dynamics over a short-term period (days to months). Further long-term validations are carried out in the following section by comparing overall SSC pattern, annual morphological changes, annual sediment transport budget, and evolution trend of the bed composition.

5. Model results and long-term validation (months to years)

5.1. Suspended sediment concentration (SSC) patterns

Fig. 8a shows the overall pattern of the annual-averaged SSC distribution based on three-year's simulation results. In general, the SSCs are high along the coast while decreasing in the seaward direction. Specifically, the concentrations in the Haizhou Bay and the deep waters (depth > 20 m) are quite low (< 0.01 kg/m³). In the area between the OYRD and the central RSRF, a high concentration band exists along the coast (with a concentration > 0.8 kg/m³). The SSCs exhibit peak values in the vicinity area of the OYRD, where the concentration can be as high as 1.2 kg/m³. In the southern RSRF the concentration is also high,

Table 3

Statistical comparison between traditional method and this study on simulation sand-silt mixed sediment transport.

		Model Efficiency (–)			Percentage Bias (%)			
Case		Haizhou Bay	OYRD	RSRF	Case	Haizhou Bay	OYRD	RSRF
		S1-S4	S5-S8	S9-S15 R1-R6				
		S1-S4	S5-S8	S9-S15 R1-R6	S1-S4	S5-S8	S9-S15 R1-R6	
summer	RF	0.08	0.63	0.44	RF	20.41	8.44	14.86
	TR	–1.55	0.18	0.37	TR	37.64	15.28	22.95
winter	RF	–4.00	0.44	–2.67	RF	45.69	9.28	23.43
	TR	–8.93	–4.98	–16.04	TR	65.11	47.65	42.64

Note: TR: case with traditional method (default settings of Delft3D). Summer means August of 2006; winter means January of 2007.

varying between 0.2 and 0.6 kg/m³.

During 2006–2007, large-scale measurements of SSCs in four seasons have been conducted along the Jiangsu coast (Xing et al., 2010). Both surface (0.2h) and bottom (0.8h) SSCs were measured by sampling methods (Fig. 8b). These measurements (i.e., surface and bottom SSCs) were converted to depth-averaged SSCs by assuming a linear concentration profile (Fig. 8b). In general, the overall distribution pattern of simulated SSCs agrees well with measured SSCs. The averaged SSCs in the survey area shown in Fig. 8b is 0.18 kg/m³, while simulation results in 0.17 kg/m³ in the same area. This indicates that the proposed model indeed have robust abilities to reproduce the observed SSCs in both patterns and magnitudes after successive simulation over years.

5.2. Morphological changes

5.2.1. Erosion and sedimentation patterns

The annual-averaged net bed level change is illustrated in Fig. 9a. The recognizable morphological changes are mainly observed in the shallow waters (depth < 20 m; see Fig. 9a). Along the coast, the morphological changes vary in different sub-regions. The bed level hardly changes in the Haizhou Bay, while it changes significantly in the OYRD. Especially, the Old Yellow River Estuary suffers severe erosion. Sedimentation occurs just close to the area with erosion. In the coastal area between the OYRD and Sheyang Estuary, a spatially distributed alternating-erosion-sedimentation pattern implies a presence of several offshore shoals, which are shaped by the strong tidal flow alongshore. This feature is in agreement with the cross-shore profile measurements reported by Zhou et al. (2014).

Over the RSRF, the erosion and sedimentation patterns are rather complicated due to the alternating ridge-channel bathymetry (Fig. 9). Wang (2014) summarized that erosion is evident in Xiyang channel, Huangshayang channel and Lanshayang channel based on comparisons between bathymetric charts and similar erosion pattern in major channels are also reproduced by the model (Fig. 9a). The boundaries of major ridges (Fig. 9b) can be identified by 3.5 m contour lines (i.e., the mean low tidal level). Fig. 9b depicts a gradual extension trend of these major ridges. Based on model results, the area of these major ridges is 1843 km² at the beginning and 2003 km² at the end of simulation, respectively, resulting in an extension rate of ~50 km²/year. Net sedimentation rate is calculated to be ~0.15 m/year in these major ridges. Therefore, the major ridges are still in growth stage in terms of both size and elevation. Wang (2014) reported that areas of major ridges are 2035 km² in 1979 and 2047 km² in 2006 according to bathymetric charts. The extension rate is estimated to be 0.4 km²/year. The differences between model and bathymetric chart are attributed to different identification methods and different averaging periods. Therefore, it is impossible to make a direct quantitative comparison, and only qualitative comparison can be made. Regarding net sedimentation pattern on major ridges, simulations show consistent results with bathymetric charts. Hence, both simulation results and measurement suggest that the ridges are continuously growing simultaneously with the deepening

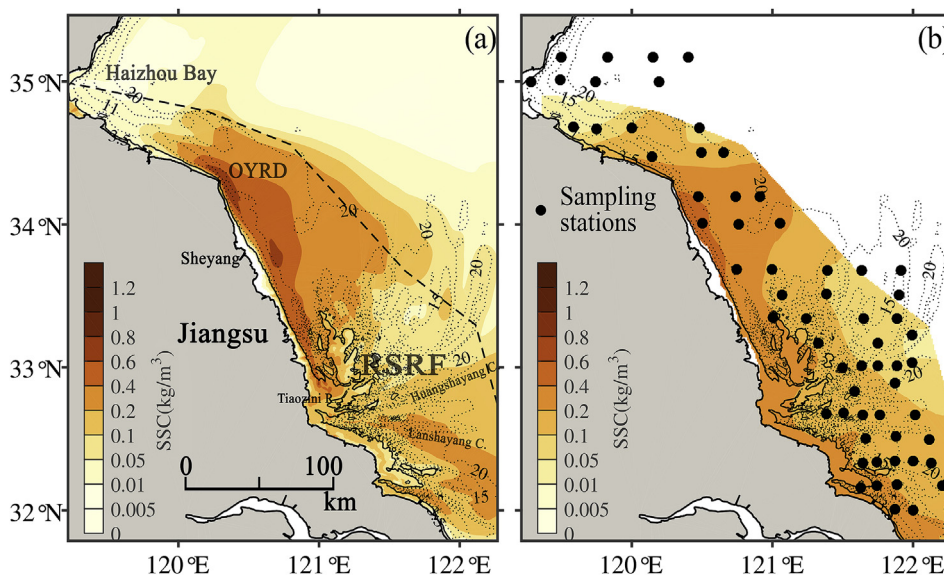


Fig. 8. Annual-averaged SSCs in the Jiangsu coastal waters: (a) modelled depth-averaged SSCs and (b) measured depth-averaged SSCs (after Xing et al., 2010). Black dots in Fig. 8b denote sampling stations on SSC measurement.

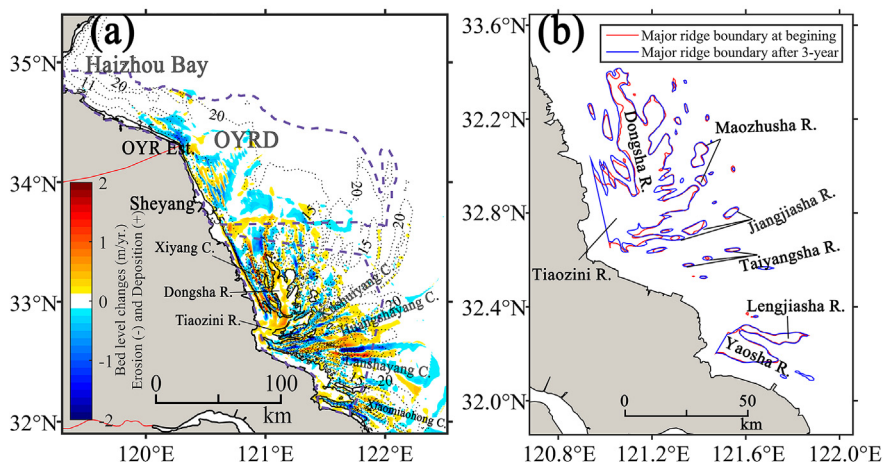


Fig. 9. Simulated annual-averaged net bed level changes (a) and changes of major ridges during 2006–2009 (b). Note: the orange colour spectrum in Fig. 9a denotes the deposition and the blue denotes the erosion. The purple dashed lines in Fig. 9a show regions for estimation of morphological volumetric changes. (For interpretation of the references to colour in this figure legend, the reader is referred to the Web version of this article.)

of the adjacent tidal channels under tidal forcing-only condition.

5.2.2. Morphological volume changes in different regions

The bathymetric measurements are the best way to assess model performance in terms of morphological volume changes. However, bathymetric data in the Jiangsu coast are rather scarce due to its complicated bathymetry and the large spatial scale. We have collected data of morphological changes within water depth of 20 m in the OYRD during a long-time span (1947–2006, Zhou et al., 2014), and bathymetric changes in the RSRF between 1979 and 2006 (Wang, 2014).

Subsequently, morphological changes based on three-year simulation results at corresponding measurement area (see Fig. 9a) were calculated in terms of annual erosion/accretion volume and net volume changes listed in Table 4. In the RSRF, simulation results show larger intensity of both annual erosion and sedimentation volumes than that according to bathymetric surveys, while annual net volume changes suggest similarities between model and measurement. In the OYRD, net erosion patterns are identified by both measurement and model, despite the model produces one-third of erosion volumes of the measurement. This can be because the annual morphological volume changes obtained by bathymetric charts were averaged in a long time period, during which sediment availability and human activities varied over time. For instance, the OYRD suffered severe erosion after 1855 due to

the cut-off of sediment supply from the Yellow River. Consequently, there has been a continuous reduction of fine materials in the OYRD (Su et al., 2017b). Thus, erosion rate produced by the model during 2006–2009 should be smaller than that of field surveys during 1947–2006. Overall, the model performance on simulating large-scale morphological changes is confirmed to be reasonable in both erosion and sedimentation patterns and morphological volume changes.

5.3. Annual tidal-induced sediment budget along the Jiangsu coast

Based on the method reported by Komar (1996), several large-scale littoral sectors are defined based on the aforementioned three featured sub-morphological units along the Jiangsu coast. The offshore boundaries of these sectors are designed to cover area where morphological changes are evident as shown in Fig. 9a. The Haizhou Bay and the OYRD are represented by Sector I and II, respectively. The area between OYRD and RSRF are represented by Sector III. Due to complex ridge-channel system in the RSRF, the whole RSRF are divided into three sectors (Sector IV–VI) from north to south. Each sector is further divided into several sub-cells to obtain more detail on the sediment transportation inside the RSRF. The tidal-induced sediment budget, i.e., the net sediment volume changes due to sediment gains and losses within each individual sector, is computed based on net sediment fluxes through

Table 4
Annual morphological volume changes in the RSRF and the OYRD: comparisons between model and data.

		RSRF		OYRD	
		Bathymetric charts comparison (1979–2006, from Wang, 2014)	3-year simulation (2006–2009)	Bathymetric charts comparison (1947–2006, from Zhou et al., 2014)	3-year simulation (2006–2009)
Sedimentation	Volume (10 ⁸ m ³ /yr)	8.22	13.71	–	5.69
	area (%)	55%	64%	–	53%
Erosion	Volume (10 ⁸ m ³ /yr)	–5.47	–11.63	–	–8.38
	area (%)	45%	36%	–	47%
Net	Volume (10 ⁸ m ³ /yr)	2.75	2.08	–8.83	–2.68

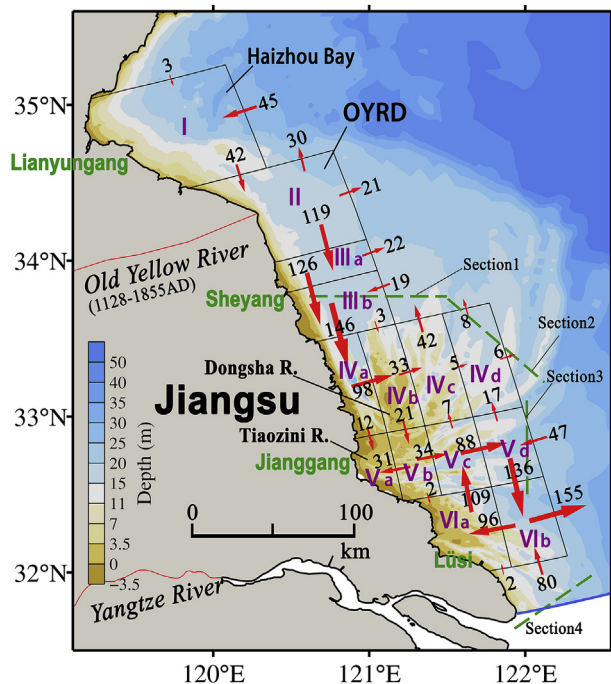


Fig. 10. Simulated large-scale tide-induced annual-averaged sediment budget in different sectors (bounded by black solid lines) along the Jiangsu coast. Unit: Mm³/year. The green dashed lines denote the transections for estimating annual sediment transport in field survey during 1980s. (For interpretation of the references to colour in this figure legend, the reader is referred to the Web version of this article.)

boundaries of each sector. Furthermore, since there is extensive area of tidal flats along the coast (Fig. 1b), sediment budget of tidal flats inside each sector are calculated to investigate their contribution. Herein, tidal flat zone is defined as the area with depth shallower than 3.5 m (i.e., mean low tidal level). The results are presented in Fig. 10 and Table 5.

The first comprehensive field survey on the RSRF was conducted in

Table 5
Annual-averaged tide-induced sediment budget per large-scale coastal sectors and per sub-regions along the Jiangsu coast. The unit is Mm³/year.

Sub-regions	Haizhou Bay (I)	OYRD (II)	Sheyang River Estuary (III)		Northern RSRF (IV)				Central RSRF (V)				Southern RSRF (VI)	
Sectors	I	II	III _a	III _b	IV _a	IV _b	IV _c	IV _d	V _a	V _b	V _c	V _d	VI _a	VI _b
Budget of Sectors	6.16	–128.58	–29.46	–4.82	35.25	47.22	–7.17	7.27	43.81	–45.97	46.76	–17.56	–8.93	–34.62
Budget of sub-regions	6.16	–128.58	–34.29		82.56				27.04				–43.55	
Budget of tidal flats	–	–	11.14		93.24				80.13				44.08	

Note that: net sediment volumes of each sector are calculated based on annual sediment fluxes (unit: m³/year) through each transection. They can be converted to amount of sediment (i.e., kg/year) by multiplying sediment density of ~2650 kg/m³. It is also possible to convert amount of sediment to morphological volume changes by dividing a dry density of materials (~1650 kg/m³ for sandy grains).

1980s (Ren, 1986). During that survey, four transections were designed to estimate annual sediment transport in the RSRF (i.e., green dashed lines in Fig. 10). Thus, series of simultaneous observations were conducted on hydrodynamics and SSCs during two tidal cycles in four seasons. The results show that sediments come into the RSRF via transections 1 (north), 3 (east) and 4 (south), while the sediments leave from the RSRF through the northeast boundary (i.e., transection 2) resulting in a net sedimentation of 186 million tons per year in the RSRF (i.e., ~70 Mm³/year by volume, see Ren, 1986 as cited in Zhang et al., 2013). Compared with the field survey, the simulation produces reasonable agreements on the sediment transport directions in corresponding transections (Fig. 10). Meanwhile, the magnitude of the net sedimentation rate in the RSRF (i.e., sum of Sector IV, V and VI, see Table 5) is estimated to be 66 Mm³/year by the model, which is in good agreement with previous observation-based estimation. Thus, the sediment budget reproduced by the long-term simulation is comparable to previous observation-based estimates, which indicates a reliable model performance on predicting of large-scale sediment transport over time scale of years.

An important issue regarding the Jiangsu coast is to identify the large-scale coastal sediment transport budget and pathways under present-day conditions. Due to the primary role of tide on sediment transport, estimation of tidal-induced sediment budget along the Jiangsu coast can provide guidelines for coastal management. Thus, annual sediment budgets as well as sediment transport pathways are identified and analysed in different coastal sub-regions as follows.

- Haizhou Bay (Sector I). Sediments are mainly input from offshore and output southward along shore to the OYRD. The budget shows a net sedimentation of ~6 Mm³/year.
- OYRD (Sector II). The area gains sediments from the northern near shore, while losing a large amount of sediments in the south and north off shore. Combining Figs. 9a and 10, the southward transport sediments are mainly from the erosion of the subaqueous delta in the OYRD. The net erosion of sediment volume is ~130 Mm³/year.
- Sheyang River Estuary (Sector III). Sediments mainly transport along shore, while in the northern estuary, cross-shore sediment output can also be observed, resulting in a net erosion of ~30 Mm³/

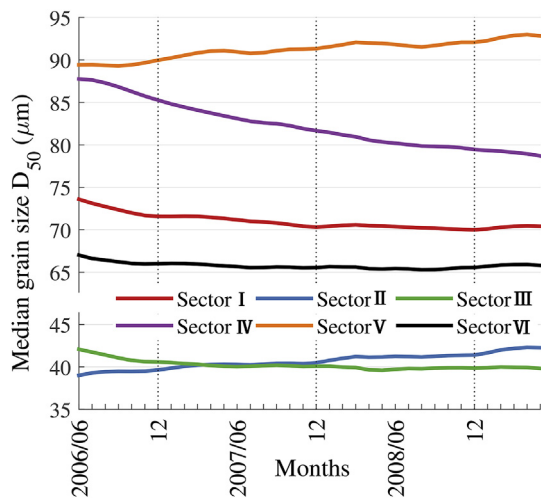


Fig. 11. Large-scale sector-averaged monthly mean median grain size (D_{50}) throughout the simulation period (i.e., three years). Different colours represent the evolution trends of different coastal sectors shown in Fig. 10. (For interpretation of the references to colour in this figure legend, the reader is referred to the Web version of this article.)

year. The sediment transport pattern in the northern part is similar to the OYRD. In the southern estuary, net volume changes are $\sim 5 \text{ Mm}^3/\text{year}$ (erosion). Overall, this area behaves as a transition zone linking the large sediment fluxes between the OYRD and Northern RSRF.

- Northern RSRF (Sector IV). A large amount of sediment is discharged into this area from north. Major part ($\sim 67\%$) of the sediments are transported across Dongsha ridge causing a net sedimentation of $\sim 50 \text{ Mm}^3/\text{year}$ there, then keeping transport seaward in the east and north direction. Minor part ($\sim 9\%$) of the sediments transport further south toward the central RSRF (i.e., Tiaozini ridge). Overall, there is a net sedimentation of $\sim 80 \text{ Mm}^3/\text{year}$ in the northern RSRF. Combining Figs. 9a and 10, the deposition is mainly distributed on the Dongsha ridge and on several small-scale ridges surrounding it, indicating the northern RSRF are still growing. Besides, it is noted that approximately 33% ($\sim 50 \text{ Mm}^3/\text{year}$) of the input sediments directly toward the north in the outer of RSRF (i.e., sub-sector IV_c and IV_d), are probably transported back to the OYRD.
- Central and southern RSRF (Sector V and VI). Sediment gains are only found in the apex area of RSRF (i.e., Tiaozini ridge) with a value of $\sim 40 \text{ Mm}^3/\text{year}$. A ∞ -pattern sediment circulation with a strong transport magnitude can be observed in the outer zone of the central RSRF and the southern RSRF (i.e., sub-sector V_c, V_d, VI_a and VI_b). Combining Figs. 9a and 10, it is found that the ∞ -pattern circulation causes a reallocation of the sediments there, i.e., accumulation on ridges and erosion in channels. Besides, in sub-sector VI_b (outer southern RSRF), the cross-shore seaward sediment transport is considerably large, i.e., $\sim 155 \text{ Mm}^3/\text{year}$. This part of sediment is not fully returned to the RSRF by the ∞ -pattern circulation, indicating a net loss of sediment in the southern RSRF.
- Tidal flats. Tidal flats along the coast are mainly distributed from Sector III to Sector VI. Despite complex erosion and sedimentation patterns in more offshore area (Fig. 9a), sediment budgets of tidal flats inside each sector all depict a net sedimentation pattern (Table 5). Therefore, tidal flats along the coast serve as a sediment sink that cumulatively accommodates sediments from surrounding area. The net sedimentation rate inside tidal flats is relatively small in the northern and southern RSRF (i.e., $10\text{--}40 \text{ Mm}^3/\text{year}$ in Sector III and VI), while much larger in the middle (i.e., $80\text{--}90 \text{ Mm}^3/\text{year}$ Sector IV and V).

The present model ability on predicting sediment transport and

morphological changes over time scale of years has been validated against a series of data shown in Section 5.2 and 5.3, respectively. Based on the validated model, the large-scale sediment transport budgets along the Jiangsu coastal waters can be identified as: erosion is found in the north (i.e., the OYRD) and in the south (i.e., southern RSRF) of the Jiangsu coast, while sedimentation is found in the central Jiangsu coast (i.e., northern and central RSRF). Tidal flats which mainly distribute in the middle and southern coast are still in sedimentation stage. In the northern coastal waters, sediments mainly exhibit the one-way transport pattern: sediments eroded from the OYRD are successively input into the northern and central RSRF. In the southern coastal waters, the regional sediment circulation (i.e., ∞ -pattern) not only reallocates internal sediments, but also leads to a net sediment loss seaward.

5.4. Temporal evolution of the bed composition

The bottom sediment availability and the fractional percentage of each sediment fraction (i.e., $16\text{-}\mu\text{m}$, $45\text{-}\mu\text{m}$, $90\text{-}\mu\text{m}$ and $180\text{-}\mu\text{m}$ fraction) are updated during simulation (with an output interval of 30 min). Therefore, the temporal evolutionary trend of the bed materials in each large-scale sector of the Jiangsu coast can be identified. We focus on the bed composition of the topmost layer (i.e., the active layer) and use the median grain size as an interpreter of bed composition. Firstly, the median grain size (D_{50}) of each computational cell are calculated based on the fractional percentage. Subsequently, the time-series median grain size at each grid cell is averaged over each month, respectively. Finally, the monthly-mean grain size is averaged within each pre-defined large-scale coastal sector (Fig. 10) and presented in Fig. 11.

In the Haizhou Bay (Sector I), the sector-averaged D_{50} first decreases then stabilizes to a more or less constant value. The adjustments of sector-averaged grain size are within $\sim 5 \mu\text{m}$, implying the prescribed bed composition reflects the realistic conditions in corresponding regions. The first reduction is because the initial bed composition does not match with the hydrodynamics, but with a certain time period, the initial mismatched bed composition can be self-adjusted (morphodynamic spin-up) towards a quasi-steady state. Similar phenomena can be found in Sector III (Sheyang Estuary) and Sector VI (southern RSRF). In these three sectors, the bed composition eventually exhibits less variation and maintains a more or less constant median grain size.

In the OYRD, the northern and the central RSRF (i.e., Sector II, IV and V), the sector-averaged D_{50} does not show the trend of 'spinning-up toward a stable state'. Instead, the sector-averaged D_{50} indicates a gradually coarsening sediment bed in the OYRD (Sector II) and central RSRF (Sector V), whereas the bed composition in the northern RSRF (Sector IV) shows a gradually fining trend. This indicates that the bed composition is still in adjustment and would not reach stable in a short period. As reported by Zhang (2016), field surveys on surface bed sediment in the OYRD have been conducted in 2008 and 2012, respectively. The corresponding data were recompiled and shown in Fig. 12a and 12b. The region-averaged median grain size (i.e., blue lines in Fig. 12a and 12b) is $\sim 6.34\Phi$ ($12 \mu\text{m}$) in 2008 and $\sim 6.17\Phi$ ($13.9 \mu\text{m}$) leading to a slightly coarsening trend ($\sim 0.5 \mu\text{m}/\text{year}$). The three-year simulation results in an overall coarsening rate ($\sim 1 \mu\text{m}/\text{year}$) in similar region, which is in line with the recent field survey. In the RSRF, due to its large scale and complex bathymetry, coherent bed composition surveys are very scarce (Wang, 2014). Sporadic field surveys in the past decades show quite low spatial resolutions on sampling surface bed sediments (see Fig. 12c and 12d). Thus, it is impossible to conduct detailed comparison between model results and measurements, and only large-scale comparison can be made by available data in the RSRF. Based on data presented in Fig. 12c and 12d, the averaged median grain size in the RSRF is 3.6Φ ($82.5 \mu\text{m}$) in 1990s and is 3.9Φ ($67 \mu\text{m}$) in 2000s. This indicates an overall fining trend in the RSRF with a rate of $\sim 1.4 \mu\text{m}/\text{year}$. In the same region, the averaged median grain size predicted by the model is $86.8 \mu\text{m}$ and $83.5 \mu\text{m}$ at the beginning and end of simulation, respectively. Thus, the present model results in a

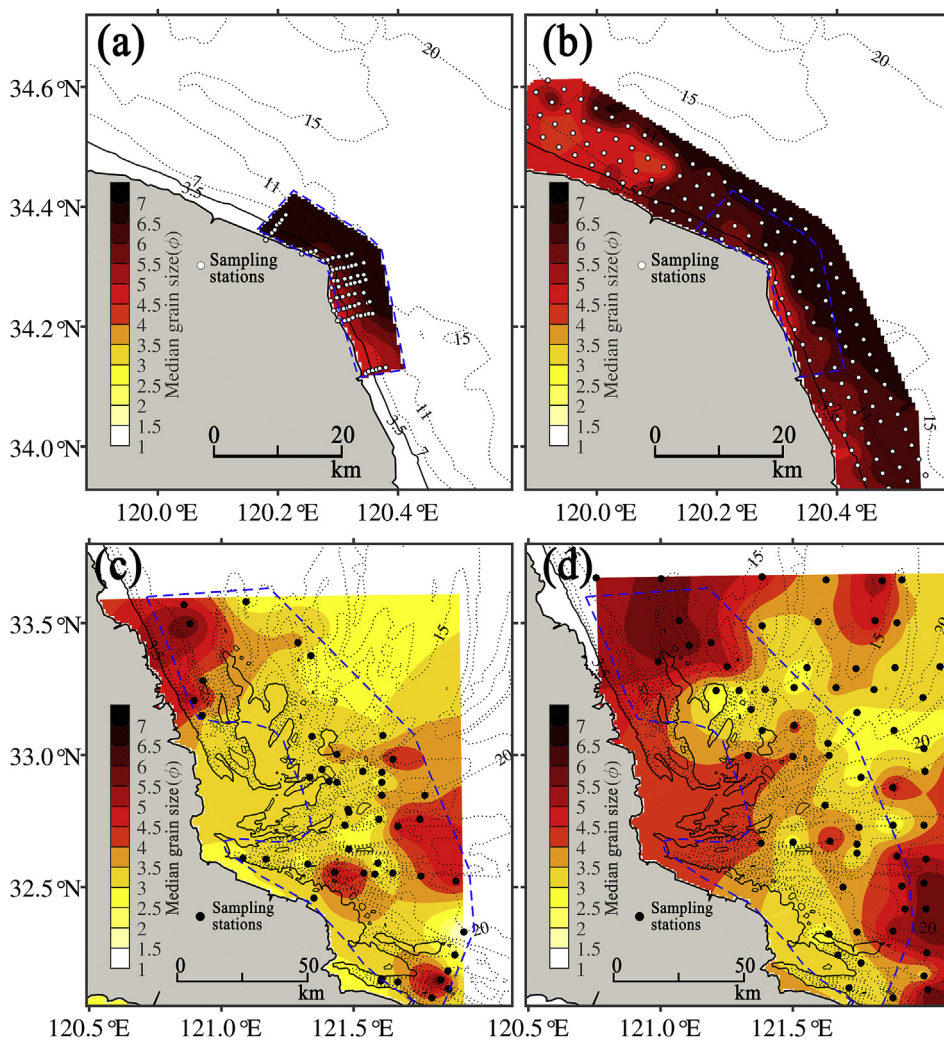


Fig. 12. Median grain size distribution of surface bed materials in the OYRD (a–b) and RSRF (c–d). Fig. 12a and 12b shows data measured in 2008 and 2012, respectively (after Zhang, 2016). Fig. 12c and 12d shows data measured in 1993–1996 and 2006–2007, respectively (after Wang, 2014). Blue lines in each figure denotes region for calculating spatial-averaged sediment size. (For interpretation of the references to colour in this figure legend, the reader is referred to the Web version of this article.)

fining trend in the RSRF (~1.1 μm/year), which agrees well with field survey. Therefore, both model and measurement indicate that sediment bed exhibits an overall coarsening trend in the OYRD, whereas the RSRF experiences an overall fining trend of the bed.

6. Discussions

6.1. Influence of Yangtze River-derived sediment

Wang et al. (2015) reviewed past studies on the influence of the Yangtze-derived sediment on the Jiangsu coast and found that there is no consensus yet. Hence, a sensitivity study is carried out in order to investigate the response of the Jiangsu coastal morphological changes (especially the southern RSRF; see Sector VI in Fig. 10) to Yangtze-derived sediment. Four cases with different inflow concentration levels (i.e., 1, 10, 100 and 300 mg/l) are designed along the southernmost open boundary. Note that the value of 100 mg/l is used in the present model and is taken as a reference value. We run the model for 45 days with the first 15 days as the spin-up period. Subsequently, we calculate the sediment budget of 30 days in the Sector VI (southern RSRF), as it is the closest region to the southern boundary. The results of each case are listed in Table 6.

It is evident that within a month, the sediment fluxes through each

Table 6

The sediment fluxes within a month through each transections of Sector VI in different sensitivity cases. Unit: Mm³/year.

Cases	C1	C2	C3	C4
Transection01 (north)	-3.5925	-3.5925	-3.5935	-3.5935
Transection02 (east)	-11.5980	-11.5990	-11.6000	-11.6000
Transection03 (south)	3.3422	3.3413	3.3411	3.3410

Note: C1 denotes the SSC at southernmost open boundary is set to 300 mg/l; C2 is 100 mg/l (this study); C3 is 10 mg/l; C4 is 1 mg/l. Different transection is corresponding to Sector VI in Fig. 10. Positive value represents the landward transport in the cross-shore direction; along-shore transport in northward direction.

transection of Sector VI are more or less the same in both magnitude and direction in all cases. Although we only carried out the simulations for one month, it is expected that the long-term influence of the SSC boundary conditions is similar. On the other hand, Su et al. (2015) found that considering the Yangtze River discharge only affects the hydrodynamics within the estuary zone (further south than a latitude of 32°) using a large-scale tidal wave model covering the Bohai Sea, Yellow Sea and part of the East China Sea. The large-scale tidal wave model also illustrates that the residual Eulerian currents near the

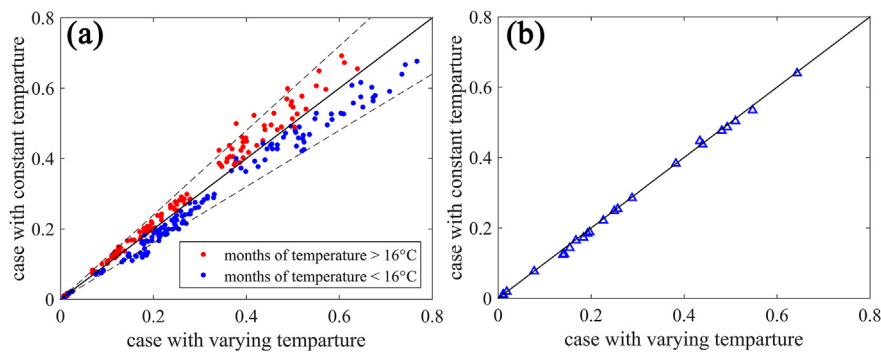


Fig. 13. Comparisons of monthly-averaged SSCs (a) and annual-averaged SSC (b) at each mooring station (shown in Fig. 1b) between caseCT and caseRF.

Yangtze Estuary are mainly directed toward the east and the southeast. Even though the SSC magnitude near the Yangtze Estuary may be high, lack of northward transport agents leads to a negligible role of the Yangtze-derived sediment on the southern Jiangsu coast morphologies. The sensitivity simulations show that Yangtze-derived sediment can hardly enter the Jiangsu coast under tidal force only. However, beside tidal induced residual sediment transport, monsoon-driven current may influence dispersion of the Yangtze plume. It is still unclear the relative contributions of the tidal-induced and wind-driven residual transport, which require further studies.

6.2. Influence of the temperature on SSCs

Impacts of temperature on SSCs over different time scale are examined by newly designed caseCT (with constant sea water temperature, i.e., 16 °C) and caseRF (with varying temperature). The simulation time of both cases is set to one year. Both annual and monthly-averaged SSCs at each station (see Fig. 1b for stations) have been compared in Fig. 13. For months with temperature larger than averaged temperature (caseCT), caseCT produces larger SSCs at all stations than caseRF, whereas caseCT leads to smaller SSCs in months with temperature smaller than 16 °C. These deviations are within 20%. This seasonal deviation is not surprising because higher temperature can result in smaller viscosity and thus larger settling velocity. For fine materials, larger settling velocity reduces suspension time in water resulting in low SSCs (Krögel and Flemming, 1998). With respect to the Jiangsu coast, sediments in suspension are mainly composed by fine grains, which is more sensitive to the temperature than coarser ones. Regarding annual averaged SSCs, cases with and without varying temperature produce in quite similar results implying temperature has little effects on annual sediment concentrations. Therefore, for modelling sediment transport over months or intra-annual, it is recommended that the temperature should be set according to the corresponding simulation period, while for modelling sediment dynamics over time scale of years or longer, it is acceptable to apply a constant averaged temperature.

6.3. Remarks for further research

6.3.1. Remarks on modelling tidal-induced sediment transport over sand-silt mixtures

The bottom sediment types, e.g. median grain sizes, compositions, etc., are of the first order significant for prediction sediment transport, since different sediment grains behave different even under same hydrodynamic forcing (Luan et al., 2017). Regarding sediment modelling in a sand-silt mixed environment, model with a spatially homogeneous cohesive muddy bed setting, cannot reproduce reliable sediment dynamics (van Kessel et al., 2011; Xu et al., 2016). Thus, a reasonable schematization of sediment bed is rather important for sediment modelling purpose. In this study, the initial bottom sediment composition was reconstructed based on previously published maps of distribution

of sediment types, together with four sediment fractions. Under this configuration, even traditional method (i.e., formulating sediment grains smaller than 62 μm by Partheniades-Krone formulations and that larger than 62 μm by non-cohesive formulations) provides reasonable results on simulation over time scale of weeks to months.

This study suggests that traditional method is applicable together with appropriate schematization of bed composition for modelling short-term sediment dynamics over sand-silt mixtures. However, traditional method can hardly be applied in time scale of months to years, because the growth of model deviation with the increase of simulation time is significant (Table 4). This further implies that the way of formulating sediment transport becomes as important as the bed compositions regarding longer simulation period. To this end, the newly integrated model with both upgraded formulations as well as reconstructed bed compositions can result in relatively robust skill from days to years over sand-silt mixed environment.

6.3.2. Remarks on effects of wind

By carrying out numerical experiments, Xing et al. (2012) found that if excluding tides, the simulated either wind-induced or other forcing-induced SSCs are as low as zero, implying the primary importance of tide on sediment re-suspension and the regional sediment transport in the Jiangsu coast. Regarding sediment transport over time scale of years, monsoon-driven coastal currents may also be important on net sediment transport. However, van der Molen (2002) suggest that wind-driven sediment transport is only active where tidal currents are weak but waves are strong. Thus, it is still unclear to what extent the monsoon-driven sediment transport can impact the sediment budget near shore. To this end, the simulation method of this study which successively predict tidal-induced sediment transport over days to years, can serve as a basis for exploring relative contributions of tidal-induced and monsoon-driven residual sediment transport.

Winds not only drive currents but also generate waves. The present model results during winter season suggest impacts of waves may become important because strong waves can exert more bed materials into suspension and increasing SSCs in several regions (Fig. 6). Xing et al. (2012) suggests that the effects of waves on the morphological changes of the Jiangsu coast are localized and have seasonal varieties, while the tides are dominant and stable throughout the whole region and the whole year. Hence, waves may influence the sediment transport in different temporal and spatial scales, but the degree of influence is unclear. This can be serving as a future research emphasis. Due to the lack of measurements on winds and waves in the Jiangsu coast, the satellite-derived global-scale wind datasets (e.g., Hoffman and Leidner, 2005; Atlas et al., 2010) and/or the global-scale reanalysis datasets (e.g., Kalnay et al., 1996) can be used to derive the wind climatology on the inner shelf along the Jiangsu coast. Subsequently, the wind climate data can be applied to drive the wave model (e.g., SWAN model) and further coupled with the flow results to compute the sediment transport as well as the morphological changes.

6.3.3. Remarks on morphodynamic modelling over years to centuries

The present modelling scheme follows a ‘brute force’ method, which is to calculate the hydrodynamics, sediment transport and the bed level changes simultaneously at same small time steps. The morphology is kept unchanged during the computation of hydrodynamics, while the hydrodynamics remain stable when calculating the morphology (Wang et al., 1995). The computation itself is a very time-consuming due to multi-fraction and multi-physical processes considered in the model, further restricting model efficiency. Since the time scales of coastal morphodynamics (e.g., OYRD and RSRF) are related to the relevant spatial scale (De Vriend, 1991), the alternation time of the OYRD and RSRF would be decades to centuries, which is further beyond simulation period of the present model. Since the morphology does not change as frequently as the flow, several strategies for accelerating the morphology updating have been proposed, such as the method of the ‘morphological factor’ (see Roelvink and Reniers, 2011 for an overview). For example, instead of really running a model through 700 tidal cycles per year, the model can only be run with several carefully selected representative tidal cycles (i.e., morphological tide), together with an acceleration factor to estimate the morphological changes over a longer period. Hence, it will be a challenge to couple the present sediment transport model (with multi-sediment fractions and bed composition) with the morphological acceleration method and schematic driving forcing, and then to produce reliable both hind- and forecast morphological results over decades or centuries; this will be a future research target. The present work can, therefore, serve as a benchmark for further developing and updating a long-term and large-scale morphodynamic (hindcast/forecast) model in the Jiangsu coastal waters as well as in other coastal regions.

7. Conclusions

We have developed a depth-averaged sediment transport module over a silt-enriched sedimentary environment with the updated formulations of van Rijn (2007a, 2007b). The sediment transport module is integrated into an open source Delft3D modelling system and then applied to the inner shelf along the Jiangsu coast. Subsequently, the model predictive ability in the real-life case is assessed on both short- and long-term scales. The model has first been calibrated and validated against two independent short-term measurement series of water level, flow velocity and suspended sediment concentration, respectively. Both

Appendix A. Supplementary data

Supplementary data to this article can be found online at <https://doi.org/10.1016/j.coastaleng.2018.09.002>.

Appendix B. Updated vRijn07 sediment transport formulations

van Rijn (1993) separated the sediment transport in two modes by a reference height (z_a): bed-load transport (below z_a); suspended load transport (above z_a). The reference height z_a is determined by (in case of current-only):

$$z_a = \max(0.5k_{s,c,r}, 0.01), \tag{A1}$$

in which, $k_{s,c,r}$ is the current-related roughness of small-scale ripples, and

$$k_{s,c,r} = \begin{cases} 150f_{cs}D_{50,bed}, & \text{for } \psi \leq 50 \\ (182.5 - 0.652\psi)f_{cs}D_{50,bed}, & \text{for } 50 < \psi \leq 250 \\ 20f_{cs}D_{50,bed}, & \text{for } \psi \geq 250 \\ 20d_{silt}, & \text{for } D_{50,bed} < d_{silt} \end{cases}, \tag{A2}$$

in which, $D_{50,bed}$ is the median grain size of the mixed bed and $D_{50,bed}$ is calculated based on the initial pre-defined sediment fractions assuming a piecewise log-uniform distribution within each sediment fraction; ψ is the mobility number for the current conditions and $\psi = u_m^2 / [(s - 1)gD_{50,bed}]$; u_m is the depth-averaged current velocity; s the relative density, and $s = \rho_s / \rho_w$; ρ_s is the sediment density; ρ_w is the water density; f_{cs} is a parameter for coarse particles, and $f_{cs} = (0.25d_{gravel} / D_{50,bed})^{1.5}$; $f_{cs} = 1$ for $D_{50,bed} \leq 0.25d_{gravel}$; $d_{silt} = 32 \mu\text{m}$ and $d_{gravel} = 2000 \mu\text{m}$.

At the reference height, the sediment concentration ($c_{a,i}$) is calculated as (in case of current-only):

the qualitative visual comparison (i.e., time-series plots) and quantitative statistical metrics (i.e., *ME* and *PB*) confirm that the present model can reproduce good results over a short-term period.

The resulting model over a short-term period (days to months) is extrapolated to simulate long-term predictions (months to years). The simulated annual-averaged SSCs indicate a high value in the coastal region between the OYRD and the northern RSRF. The simulated morphological changes show a spatially distributed alternating-erosion-sedimentation pattern in the southern OYRD. Over the RSRF, the ridges are continuously growing while the adjacent tidal channels are deepening. The simulated tide-induced sediment budget suggests that the northern (i.e., the OYRD) and southern (i.e., the southern RSRF) Jiangsu coasts are under erosion, while the central coast (i.e., the northern and central RSRF) is still in a state of accumulation. Furthermore, the sediment bed in the OYRD shows a gradually coarsening trend while an overall fining trend is pronounced in the northern RSRF. All these long-term trends of the simulated sediment dynamics are in good agreement with observation-based estimations. Moreover, this study suggests that under tidal force only, the influence of the Yangtze River delivered sediment can hardly influence sediment dynamics of Jiangsu coast.

With application to the Jiangsu coastal waters, the ability of the present model has been confirmed regarding to the simulation of sediment transport, bed composition alternation as well as bed level change in a sand-silt mixed sediment environment. Although the secondary forcing agents such as the waves and winds are excluded in this application and require further verifications, the results still indicate a good model capability for successive simulation from days to years. The present model can serve as a basis for studying long-term sediment transport under various forcing as well as investigating morphological evolution trend over years to centuries.

Acknowledgments

This work was supported by the National Natural Science Foundation of China (Grant No. 51620105005, 51520105014 and 51709288), the Open Foundation of State Key Laboratory of Hydrology-Water Resources and Hydraulic Engineering (Grant No. 2016491711 and 2017491311), the Open Foundation of State Key Laboratory of Ocean Engineering (Grant No. 1706). We thank Drs. Mariette van Tilburg for checking the manuscript.

$$c_{a,i} = \beta \rho_s p_i f_{silt,i} \frac{D_i T_i^{1.5}}{z_a D_{*,i}^{0.3}}, \quad (A3)$$

where, β is an empirical coefficient and $\beta = 0.015$ in current-only conditions; $f_{silt,i}$ is a silt factor, and $f_{silt,i} = d_{sand}/D_i$ ($f_{silt} = 1$ for $D_i > d_{sand} = 62 \mu\text{m}$); D_i is the median grain size of fraction i ; p_i is the relative availability (i.e., percentage) of sediment fraction i in the sediment bed and p_i is updated during simulation; $D_{*,i}$ is the dimensionless particle size and $D_{*,i} = D_i [(s-1)g/\nu^2]^{1/3}$; ν is the kinematic viscosity coefficient; T_i is the excess bed shear stress given by,

$$T_i = \frac{(\tau'_i - \tau_{cr,i})}{\tau_{cr,i}}, \quad (A4)$$

where, the subscript i represents the corresponding coefficient of the sediment fraction i ; $\tau_{cr,i}$ is the critical bed shear stress; τ'_i is the effective bed-shear stress under currents and $\tau'_i = \mu_{c,i} \tau$; $\mu_{c,i}$ is the efficiency factor of current and $\mu_{c,i} = f'_{c,i}/f_c$; f_c is the total current-related friction factor and $f_c = 0.24 \log_{10}(12h/k_{s,c})^{-2}$; $f'_{c,i}$ is the grain related friction factor and $f'_{c,i} = 0.24 \log_{10}(12h/k_{s,grain,i})^{-2}$; τ is the total current-related bed shear stress; $k_{s,c}$ is the current-related bed roughness and is predicted as a quadratic summation of roughness due to small-scale ripples ($k_{s,c,r}$) and mega-scale ripples ($k_{s,c,mr}$) as $k_{s,c} = \sqrt{k_{s,c,r}^2 + k_{s,c,mr}^2}$. For the calculation of the roughness due to mega-ripples, the readers are referred to van Rijn (2007a). It is noted that in the present study, the total physical current-related bed shear stress (τ) does not directly take from the flow results (i.e., traditional approach), but is calculated individually by:

$$\tau = 0.125 \rho_w f_c u_m^2. \quad (A5)$$

For a well-mixed bed, the grain-related roughness ($k_{s,grain,i}$) is assumed to be represented by $\alpha D_{90,bed}$ (van Rijn, 2007c), which implies a constant grain-related roughness for all fractions. Note that $D_{90,bed}$ is referred to the mixed bed. The results of our previous flume experiments indicated that the assumption produced reasonable results with $\alpha = 1$ for the sand-silt mixtures (Yao et al., 2015). Therefore, the method is implemented in the present model.

The critical bed shear stress ($\tau_{cr,bed}$) is calculated based on the median grain size of the mixed bed ($D_{50,bed}$):

$$\tau_{cr,bed} = \begin{cases} (c_{gel}/c_{gel,s})(d_{sand}/D_{50,bed})^\gamma \tau_{cr}, & \text{for } D_{50,bed} < 62 \mu\text{m (Silt range)} \\ (1 + p_{clay})^3 \tau_{cr}, & \text{for } D_{50,bed} \geq 62 \mu\text{m (Sand range)} \end{cases}, \quad (A6)$$

in which, c_{gel} is the gelling mass concentration of the finer particles, and $c_{gel} = (D_{50,bed}/D_{sand})c_{gel,s}$, with $c_{gel,min} = 120 \text{ kg/m}^3$ (mass, or 0.05 as dry bulk density by volume); $c_{gel,s}$ is the dry bulk density of sand bed by mass (1722 kg/m^3 , or $(1-\eta) = 0.65$ as dry bulk density by volume); η is the porosity of the sand bed ($\eta \approx 0.35$ for pure sand bed); γ is the empirical coefficient, in the range of 1–2 (1.5 is selected in the present study); τ_{cr} is the original critical bed shear stress based on a parametric Shields curve:

$$\frac{\tau_{cr}}{[(\rho_s - \rho_w)gD_{50,bed}]} = \begin{cases} 0.115D_*^{-0.5}, & 1 < D_* \leq 4 \\ 0.14D_*^{-0.64}, & 4 < D_* \leq 10 \\ 0.04D_*^{-0.1}, & 10 < D_* \leq 20, \\ 0.013D_*^{0.29}, & 20 < D_* \leq 150 \\ 0.055, & 150 < D_* \end{cases} \quad (A7)$$

where, D_* is dimensionless particle size of the mixed bed (i.e., based on $D_{50,bed}$).

Subsequently, the critical bed shear stress of each fraction ($\tau_{cr,i}$) is calculated based on $\tau_{cr,bed}$ with consideration of hiding and exposure effects (Kleinhans and van Rijn, 2002). The hiding and exposure effects are taken into account by increasing the critical shear stress for the finer fraction while decreasing it for the coarser fraction. This adjustment is carried out by multiplying a parameter ξ_j . In the present modelling method, the hiding and exposure effects are active for $D_{50,bed} > 40 \mu\text{m}$. Yao et al. (2015) suggested the theoretical function of Egiazaroff (1965) gives a better estimation on the silt-enriched mixtures:

$$\xi_i = \left[\frac{\log_{10}(19)}{\log_{10}(19D_i/D_{50,bed})} \right]^2. \quad (A8)$$

Consequently, the critical bed shear stress of each fraction ($\tau_{cr,i}$) is calculated by $\tau_{cr,i} = \xi_i (D_i/D_{50,bed}) \tau_{cr,bed}$.

The current-related sediment mixing coefficient $\varepsilon_{s,c}$ is calculated based on a ‘parabolic-constant’ distribution shape:

$$\varepsilon_{s,c,i} = \begin{cases} \kappa \beta_{c,i} u_{*,c} z(1-z/h), & \text{when } z < 0.5h \\ 0.25 \kappa \beta_{c,i} u_{*,c} h, & \text{when } z \geq 0.5h \end{cases}, \quad (A9)$$

where, κ is the Von Karman constant (0.4); $u_{*,c}$ is the current-related bed-shear velocity; $\beta_{c,i} = 1 + 2(w_{s,i}/u_{*,c})^2$ and $\beta_{c,i} \leq 1.5$. The turbulence damping by stratification effects of high concentration layer is considered by a damping factor ϕ_d , which is expressed as:

$$\phi_d = \phi_{fs} [1 + (c_t/c_{gel,s})^{0.8} - 2(c_t/c_{gel,s})^{0.4}], \quad (A10)$$

in which, c_t is the total sediment concentration at the height z ; ϕ_{fs} is a calibration factor considering the effect of fine particles for the nature sand-silt-clay mixtures, and $\phi_{fs} = D_{50,bed}/(1.5d_{sand})$ ($\phi_{fs} = 1$, for $D_{50,bed} \geq 1.5d_{sand}$).

The settling velocity ($w_{s,i}$) is directly related to the median particle size (D_i) of each fraction:

$$w_{s,i} = \begin{cases} \frac{vD_{*i}^3}{18D_i}, & \text{for } D_{*i}^3 \leq 16.187 \\ \frac{10v}{D_i} [(1 + 0.01D_{*i}^3)^{1/2} - 1], & \text{for } 16.187 < D_{*i}^3 \leq 16187. \\ \frac{1.1vD_{*i}^{1.5}}{D_i}, & \text{for } D_{*i}^3 > 16187 \end{cases} \quad (\text{A11})$$

Hindered settling effect on settling velocity is taken into account by multiplying a parameter of:

$$\phi_{hs} = (1 - 0.65c_t/c_{gel})^5. \quad (\text{A12})$$

The flocculation is active for finer materials in the salinity environment considered by multiplying a parameter of:

$$\phi_{floc} = [4 + \log_{10}(2c_{tf}/c_{gel})]^\alpha, \quad (\text{A13})$$

in which, $\alpha = (d_{sand}/D_i) - 1$ with $\alpha_{min} = 0$ and $\alpha_{max} = 3$; c_{tf} is the sum of the mass concentration of finer fractions ($D_i < 40 \mu\text{m}$). Note that the flocculation is only considered for $D_i < 40 \mu\text{m}$ in this study.

The bed slope may affect the sediment transport in the following two ways: changing the threshold conditions of initiation of motion; changing the bed-load transport rate (in case the sediment is in motion). The influence of the bed slope on critical bed shear stress is considered by a sloping factor (Dey, 2001; van Rijn, 1993),

$$\phi_{slope} = (1 - \beta/\varphi)^{0.78}(1 - \gamma/\varphi)^{0.37}, \quad (\text{A14})$$

where, β is the longitudinal bed slope angle; γ is the lateral bed slope angle; φ is the angle of repose.

The influence of the bed slope on the bed-load transport rate is considered by multiplying a correction coefficient α_s in s -direction (i.e., initial transport direction; see Bagnold, 1956) and an additional coefficient α_n in n -direction (normal to s -direction; see Ikeda, 1982):

$$\alpha_s = 1 + \alpha_{bs}\{\tan \varphi / [\cos \beta (\tan \varphi - \tan \beta)] - 1\}, \quad (\text{A15})$$

in which, α_{bs} is the tuning parameter ($\alpha_{bs} = 1$ in this study). And,

$$\alpha_n = \alpha_{bn}(\tau_{cr,b}/\tau_b)^{0.5} \tan \gamma, \quad (\text{A16})$$

in which, α_{bn} is the tuning parameter ($\alpha_{bn} = 1.5$ in this study). For more information, see van Rijn (2006).

References

- Alexander, C.R., DeMaster, D.J., Nittrouer, C.A., 1991. Sediment accumulation in a modern epicontinental-shelf setting: the Yellow Sea. *Mar. Geol.* 98, 51–72. [https://doi.org/10.1016/0025-3227\(91\)90035-3](https://doi.org/10.1016/0025-3227(91)90035-3).
- Allen, J.I., Somerfield, P.J., Gilbert, F.J., 2007. Quantifying uncertainty in high-resolution coupled hydrodynamic-ecosystem models. In: *Journal of Marine Systems*, Contributions from Advances in Marine Ecosystem Modelling Research, 27–29 June, 2005. AMEMR 64, Plymouth, UK, pp. 3–14. <https://doi.org/10.1016/j.jmarsys.2006.02.010>.
- Amoudry, L.O., Ramirez-Mendoza, R., Souza, A.J., Brown, J.M., 2014. Modelling-based assessment of suspended sediment dynamics in a hypertidal estuarine channel. *Ocean Dynam.* 64, 707–722. <https://doi.org/10.1007/s10236-014-0695-8>.
- Atlas, R., Hoffman, R.N., Ardizzone, J., Leidner, S.M., Jusem, J.C., Smith, D.K., Gombos, D., 2010. A cross-calibrated, multiplatform ocean surface wind velocity product for meteorological and oceanographic applications. *Bull. Am. Meteorol. Soc.* 92, 157–174. <https://doi.org/10.1175/2010BAMS2946.1>.
- Bagnold, R.A., 1956. The flow of cohesionless grains in fluids. *Phil. Trans. Roy. Soc. Lond.: Math. Phys. Eng. Sci.* 249, 235–297. <https://doi.org/10.1098/rsta.1956.0020>.
- Blaas, M., Dong, C., Marchesiello, P., McWilliams, J.C., Stolzenbach, K.D., 2007. Sediment-transport modeling on Southern Californian shelves: a ROMS case study. *Contin. Shelf Res.* 27, 832–853. <https://doi.org/10.1016/j.csr.2006.12.003>.
- Carniello, L., Defina, A., D'Alpaos, L., 2012. Modeling sand-mud transport induced by tidal currents and wind waves in shallow microtidal basins: application to the Venice Lagoon (Italy). *Estuar. Coast Shelf Sci.* 102–103, 105–115. <https://doi.org/10.1016/j.ecss.2012.03.016>.
- Carniello, L., Silvestri, S., Marani, M., D'Alpaos, A., Volpe, V., Defina, A., 2014. Sediment dynamics in shallow tidal basins: in situ observations, satellite retrievals, and numerical modeling in the Venice Lagoon. *J. Geophys. Res. Earth Surf.* 119, 2013JF003015. <https://doi.org/10.1002/2013JF003015>.
- Choi, B.H., 1984. A three-dimensional model of the east China sea. In: Ichiye, T. (Ed.), *Elsevier Oceanography Series, Ocean Hydrodynamics of the Japan and East China Seas*. Elsevier, pp. 209–224.
- Collins, M.B., Balson, P.S., 2007. Coastal and shelf sediment transport: an introduction. In: Balson, P.S., Collins, M.B. (Eds.), *Coastal and Shelf Sediment Transport*. Geological Society Special Publication. Geological Society, London, UK, pp. 1–5.
- De Vriend, H.J., 1991. Mathematical modelling and large-scale coastal behaviour. Part 1: physical processes. *J. Hydraul. Res.* 29, 727–740.
- Deltares, 2011. Delft3D-FLOW User Manual. 3.15 ed. ed. Deltares (WL), Delft, The Netherlands.
- Dey, S., 2001. Experimental study on incipient motion of sediment particles on generalized sloping fluvial beds. *Int. J. Sediment Res.* 16, 391–398.
- Dronkers, J., 1986. Tidal asymmetry and estuarine morphology. *Neth. J. Sea Res.* 20, 117–131. [https://doi.org/10.1016/0077-5799\(86\)90036-0](https://doi.org/10.1016/0077-5799(86)90036-0).
- Dyer, K.R., 1986. *Coastal and Estuarine Sediment Dynamics*. Wiley.
- Dyer, K.R., Huntley, D.A., 1999. The origin, classification and modelling of sand banks and ridges. *Contin. Shelf Res.* 19, 1285–1330. [https://doi.org/10.1016/S0278-4343\(99\)00028-X](https://doi.org/10.1016/S0278-4343(99)00028-X).
- Egiazaroff, I.V., 1965. Calculation of nonuniform sediment concentrations. *J. Hydraul. Div. Am. Soc. Civ. Eng.* 91, 225–247.
- Fagherazzi, S., Overeem, I., 2007. Models of deltaic and inner continental shelf landform evolution. *Annu. Rev. Earth Planet Sci.* 35, 685–715. <https://doi.org/10.1146/annurev.earth.35.031306.140128>.
- Falconer, R.A., Owens, P.H., 1990. Numerical modelling of suspended sediment fluxes in estuarine waters. *Estuar. Coast Shelf Sci.* 31, 745–762. [https://doi.org/10.1016/0272-7714\(90\)90080-B](https://doi.org/10.1016/0272-7714(90)90080-B).
- Fang, G., 1986. Tide and tidal current charts for the marginal seas adjacent to China. *Chin. J. Oceanol. Limnol.* 4, 1–16. <https://doi.org/10.1007/BF02850393>.
- Fitzpatrick, J.J., 2009. Assessing skill of estuarine and coastal eutrophication models for water quality managers. *J. Mar. Syst.* 76, 195–211. Skill assessment for coupled biological/physical models of marine systems. <https://doi.org/10.1016/j.jmarsys.2008.05.018>.
- Galappatti, R., 1983. *A Depth Integrated Model for Suspended Transport*. Delft University of Technology, Delft, the Netherlands.
- Gao, S., 2009. Modeling the preservation potential of tidal flat sedimentary records, Jiangsu coast, eastern China. *Contin. Shelf Res. Special issue in honour of Michael Collins* 29, 1927–1936. <https://doi.org/10.1016/j.csr.2008.12.010>.
- Greenwood, B., Xu, Z., 2001. Size fractionation by suspension transport: a large scale flume experiment with shoaling waves. *Mar. Geol.* 176, 157–174. [https://doi.org/10.1016/S0025-3227\(01\)00159-1](https://doi.org/10.1016/S0025-3227(01)00159-1).
- Guo, L., van der Wegen, M., Roelvink, D., He, Q., 2015. Exploration of the impact of seasonal river discharge variations on long-term estuarine morphodynamic behavior. *Coast Eng.* 95, 105–116. <https://doi.org/10.1016/j.coastaleng.2014.10.006>.
- He, X.Y., Hu, T., Wang, Y.P., Zou, X.Q., Shi, X.Z., 2010. Seasonal distributions of hydrometeor parameters in the offshore sea of Jiangsu. *Mar. Sci.* 34, 44–54.
- Hirano, M., 1971. River bed degradation with armouring. *Trans. Jpn. Soc. Civ. Eng.* 3, 194–195.
- Hoffman, R.N., Leidner, S.M., 2005. An introduction to the near-real-time QuikSCAT data. *Weather Forecast.* 20, 476–493. <https://doi.org/10.1175/WAF841.1>.
- Hooshmand, A., Horner-Devine, A.R., Lamb, M.P., 2015. Structure of turbulence and sediment stratification in wave-supported mud layers. *J. Geophys. Res. Oceans* 120, 2430–2448. <https://doi.org/10.1002/2014JC010231>.
- Ikeda, S., 1982. Lateral bed load transport on side slopes. *J. Hydraul. Div.* 108, 1369–1373.
- Jacobs, W., Le Hir, P., Van Kesteren, W., Cann, P., 2011. Erosion threshold of sand–mud mixtures. *Continental Shelf Research, Proceedings of the 9th International Conference on Nearshore and Estuarine Cohesive Sediment Transport Processes*, vol. 31, pp. S14–S25. <https://doi.org/10.1016/j.csr.2010.05.012>.
- Kalnay, E., Kanamitsu, M., Kistler, R., Collins, W., Deaven, D., Gandin, L., Iredell, M., Saha, S., White, G., Woollen, J., Zhu, Y., Leetmaa, A., Reynolds, R., Chelliah, M., Ebisuzaki, W., Higgins, W., Janowiak, J., Mo, K.C., Ropelewski, C., Wang, J., Jenne, R., Joseph, D., 1996. The NCEP/NCAR 40-year reanalysis project. *Bull. Am. Meteorol.*

- Soc. 77, 437–471. [https://doi.org/10.1175/1520-0477\(1996\)077<0437:TNYRP>2.CO;2](https://doi.org/10.1175/1520-0477(1996)077<0437:TNYRP>2.CO;2).
- Kleinhans, M., van Rijn, L., 2002. Stochastic prediction of sediment transport in sand-gravel bed rivers. *J. Hydraul. Eng.* 128, 412–425. [https://doi.org/10.1061/\(ASCE\)0733-9429\(2002\)128:4\(412\)](https://doi.org/10.1061/(ASCE)0733-9429(2002)128:4(412)).
- Komar, P.D., 1996. The budget of littoral sediments—Concepts and Applications. *Shore Beach* 64, 18–25.
- Krögel, F., Flemming, B.W., 1998. Evidence for Temperature-adjusted Sediment Distributions in the Back-barrier Tidal Flats of the East Frisian Wadden Sea (southern North Sea).
- Lamb, M.P., Parsons, J.D., 2005. High-density suspensions formed under waves. *J. Sediment. Res.* 75, 386–397. <https://doi.org/10.2110/jsr.2005.030>.
- Lambe, T.W., Whitman, R.V., 1979. *Soil Mechanics*, SI Version. Wiley.
- Le Hir, P., Cayocca, F., Waeles, B., 2011. Dynamics of sand and mud mixtures: a multi-process-based modelling strategy. In: *Continental Shelf Research, Proceedings of the 9th International Conference on Nearshore and Estuarine Cohesive Sediment Transport Processes* 31, pp. S135–S149. <https://doi.org/10.1016/j.csr.2010.12.009>.
- Le Hir, P., Ficht, A., Jacinto, R.S., Lesueur, P., Dupont, J.-P., Lafite, R., Brenon, I., Thouvenin, B., Cugier, P., 2001. Fine sediment transport and accumulations at the mouth of the Seine estuary (France). *Estuaries* 24, 950–963. <https://doi.org/10.2307/1353009>.
- Lee, H.J., Chough, S.K., 1989. Sediment distribution, dispersal and budget in the Yellow Sea. *Mar. Geol.* 87, 195–205.
- Lesser, G.R., Roelvink, J.A., van Kester, J.A.T.M., Stelling, G.S., 2004. Development and validation of a three-dimensional morphological model. *Coast. Eng.* 51, 883–915. <https://doi.org/10.1016/j.coastaleng.2004.07.014>.
- Liu, X.J., Gao, S., Wang, Y.P., 2011. Modeling profile shape evolution for accreting tidal flats composed of mud and sand: a case study of the central Jianguo coast, China. *Continent. Shelf Res.* 31, 1750–1760. <https://doi.org/10.1016/j.csr.2011.08.002>.
- Liu, Z., Huang, Y., Zhang, Q., 1989. Tidal current ridges in the southwestern Yellow Sea. *J. Sediment. Res.* 59, 432–437. <https://doi.org/10.1306/212F8FB7-2B24-11D7-864800102C1865D>.
- Luan, H.L., Ding, P.X., Wang, Z.B., Ge, J.Z., 2017. Process-based morphodynamic modeling of the Yangtze Estuary at a decadal timescale: controls on estuarine evolution and future trends. *Geomorphology* 290, 347–364. <https://doi.org/10.1016/j.geomorph.2017.04.016>.
- Mehta, A.J., Lee, S.-C., 1994. Problems in linking the threshold condition for the transport of cohesionless and cohesive sediment grain. *J. Coast Res.* 10, 170–177.
- Milliman, J.D., Fan, L., Yiyang, Z., Tiemin, Z., Limeburner, R., 1986. Suspended matter regime in the Yellow sea. *Prog. Oceanogr.* 17, 215–227. [https://doi.org/10.1016/0079-6611\(86\)90045-5](https://doi.org/10.1016/0079-6611(86)90045-5).
- Mitchener, H., Torfs, H., 1996. Erosion of mud/sand mixtures. *Coast Eng.* 29, 1–25. [https://doi.org/10.1016/S0378-3839\(96\)00002-6](https://doi.org/10.1016/S0378-3839(96)00002-6).
- Nielsen, P., 1992. *Coastal Bottom Boundary Layers and Sediment Transport*. World Scientific.
- Partheniades, E., 1965. Erosion and deposition of cohesive soils. *J. Hydraul. Div.* 91, 105–139.
- Ren, M. (Ed.), 1986. *The Comprehensive Investigative Report on the Resources of the Coastal Zone and Tidal Flats of Jianguo Province*. China Ocean Press, Beijing.
- Ren, M.E., Shi, Y.L., 1986. Sediment discharge of the Yellow River (China) and its effect on the sedimentation of the Bohai and the Yellow sea. *Continent. Shelf Res.* 6, 785–810. [https://doi.org/10.1016/0278-4343\(86\)90037-3](https://doi.org/10.1016/0278-4343(86)90037-3).
- Roelvink, D., Reniers, A., 2011. A guide to modeling coastal morphology. *Advances in Coastal and Ocean Engineering*. World Scientific.
- Saito, Y., Yang, Z., Hori, K., 2001. The Huanghe (Yellow River) and Changjiang (Yangtze River) deltas: a review on their characteristics, evolution and sediment discharge during the Holocene. *Geomorphology* 41 (2–3), 219–231. [https://doi.org/10.1016/S0169-555X\(0100118-0\)](https://doi.org/10.1016/S0169-555X(0100118-0)).
- Shepard, F.P., 1954. Nomenclature based on sand-silt-clay ratios. *J. Sediment. Res.* 24.
- Shi, X., Liu, Y., Chen, Z., Wei, J., Ge, S., 2012. Origin, transport processes and distribution pattern of modern sediments in the Yellow Sea. *Sediments, Morphology and Sedimentary Processes on Continental Shelves: Advances in technologies, Research and Applications (Special Publication 44 of the IAS)* 44, 321–350.
- Soulsby, R., 1997. *Dynamics of Marine Sands: a Manual for Practical Applications*. Thomas Telford.
- Su, M., Yao, P., Wang, Z.B., Zhang, C.K., Stive, M.J.F., 2017a. Exploratory morphodynamic hindcast of the evolution of the abandoned Yellow River delta, 1578–1855 CE. *Mar. Geol.* 383, 99–119. <https://doi.org/10.1016/j.margeo.2016.11.007>.
- Su, M., Yao, P., Wang, Z.B., Zhang, C.K., Stive, M.J.F., 2017b. Exploratory morphodynamic modeling of the evolution of the Jianguo coast, China, since 1855: contributions of old Yellow River-derived sediment. *Mar. Geol.* 390, 306–320. <https://doi.org/10.1016/j.margeo.2016.10.013>.
- Su, M., Yao, P., Wang, Z.B., Zhang, C.K., Stive, M.J.F., 2015. Tidal wave propagation in the Yellow sea. *Coast Eng. J.* 57 1550008-1-155008-29. <https://doi.org/10.1142/S0578563415500084>.
- Sutherland, J., Peet, A.H., Soulsby, R.L., 2004. Evaluating the performance of morphological models. *Coastal Eng., Coastal Morphodyn. Model.* 51, 917–939. <https://doi.org/10.1016/j.coastaleng.2004.07.015>.
- te Slaat, S., He, Q., van Maren, D.S., Winterwerp, J.C., 2013. Sedimentation processes in silt-rich sediment systems. *Ocean Dynam.* 63, 399–421. <https://doi.org/10.1007/s10236-013-0600-x>.
- Uncles, R.J., 2002. Estuarine physical processes research: some recent studies and progress. *Estuar. Coast Shelf Sci.* 55, 829–856. <https://doi.org/10.1006/ecss.2002.1032>.
- van der Molen, J., 2002. The influence of tides, wind and waves on the net sand transport in the North Sea. *Continent. Shelf Res.* 22, 2739–2762. [https://doi.org/10.1016/S0278-4343\(02\)00124-3](https://doi.org/10.1016/S0278-4343(02)00124-3).
- van der Wegen, M., Dastgheib, A., Jaffe, B.E., Roelvink, D., 2010. Bed composition generation for morphodynamic modeling: case study of San Pablo Bay in California, USA. *Ocean Dynam.* 61, 173–186. <https://doi.org/10.1007/s10236-010-0314-2>.
- van der Wegen, M., Wang, Z.B., Savenije, H.H.G., Roelvink, J.A., 2008. Long-term morphodynamic evolution and energy dissipation in a coastal plain, tidal embayment. *J. Geophys. Res.: Earth Surf.* 113, F03001. <https://doi.org/10.1029/2007JF000898>.
- van Kessel, T., Vanlede, J., de Kok, J., 2011. Development of a mud transport model for the Scheldt estuary. *Continental Shelf Research, Proceedings of the 9th International Conference on Nearshore and Estuarine Cohesive Sediment Transport Processes*, vol. 31, pp. S165–S181. <https://doi.org/10.1016/j.csr.2010.12.006>.
- van Ledden, M., Wang, Z.B., Winterwerp, H., Vriend, H. de, 2006. Modelling sand–mud morphodynamics in the Friesche Zeegat. *Ocean Dynam.* 56, 248–265. <https://doi.org/10.1007/s10236-005-0055-9>.
- van Rijn, L.C., 2007a. Unified view of sediment transport by currents and waves. I: initiation of motion, bed roughness, and bed-load transport. *J. Hydraul. Eng.* 133, 649–667. [https://doi.org/10.1061/\(ASCE\)0733-9429\(2007\)133:6\(649\)](https://doi.org/10.1061/(ASCE)0733-9429(2007)133:6(649)).
- van Rijn, L.C., 2007b. Unified view of sediment transport by currents and waves. II: suspended transport. *J. Hydraul. Eng.* 133, 668–689. [https://doi.org/10.1061/\(ASCE\)0733-9429\(2007\)133:6\(668\)](https://doi.org/10.1061/(ASCE)0733-9429(2007)133:6(668)).
- van Rijn, L.C., 2007c. Unified view of sediment transport by currents and waves. III: graded beds. *J. Hydraul. Eng.* 133, 761–775. [https://doi.org/10.1061/\(ASCE\)0733-9429\(2007\)133:7\(761\)](https://doi.org/10.1061/(ASCE)0733-9429(2007)133:7(761)).
- van Rijn, L.C., 2006. *Principles of Sediment Transport in Rivers, Estuaries and Coastal Seas Part 2, supplement/update*. Aqua publications, Amsterdam.
- van Rijn, L.C., 1993. *Principles of Sediment Transport in Rivers, Estuaries and Coastal Seas Part 1*. Aqua publications.
- van Rijn, L.C., Grasmeyer, B.T., Ruessink, B.G., 2000. *Measurement Errors of Instruments for Velocity, Wave Height, Sand Concentration and Bed Levels in Field Conditions*. Deltares (WL) - Utrecht University, Delft, the Netherlands.
- van Rijn, L.C., Walstra, D.J.R., Grasmeyer, B., Sutherland, J., Pan, S., Sierra, J.P., 2003. The predictability of cross-shore bed evolution of sandy beaches at the time scale of storms and seasons using process-based Profile models. *Coast Eng.* 47, 295–327. [https://doi.org/10.1016/S0378-3839\(02\)00120-5](https://doi.org/10.1016/S0378-3839(02)00120-5).
- Waeles, B., Hir, P.L., Lesueur, P., 2008. A 3D Morphodynamic Process-based Modelling of a Mixed Sand/mud Coastal Environment: the Seine Estuary, France.
- Wan, X.N., Li, J.F., Shen, H.T., 2005. Suspended sediment flux at the typical cross sections in the offshore area of Changjiang Estuary. *J. Sedi. Res.* 64–70.
- Wang, R., Zhang, Y.Z., Xia, F., Zhao, S.D., 2012. Grain size distribution and transportation trends of bottom sediments in the sand ridge field of the South Yellow Sea, China. *Mar. Geol. Quat. Geol.* 32, 1–8. <https://doi.org/10.3724/SP.J.1140.2012.06001>.
- Wang, X., Ke, X., 1997. Grain-size characteristics of the extant tidal flat sediments along the Jianguo coast, China. *Sediment. Geol.* 112, 105–122. [https://doi.org/10.1016/S0037-0738\(97\)00026-2](https://doi.org/10.1016/S0037-0738(97)00026-2).
- Wang, Y., 2014. *Environment and Resources in the Radial Sand Ridge, South Yellow Sea*, first ed. Ocean Press, Beijing.
- Wang, Y., 2002. *Radiative Sandy Ridge Field on Continental Shelf of the Yellow Sea*, first ed. China Environmental Science Press, Beijing.
- Wang, Y., Zhang, Y., Zou, X., Zhu, D., Piper, D., 2012. The sand ridge field of the South Yellow Sea: origin by river–sea interaction. *Mar. Geol.* 291–294, 132–146. <https://doi.org/10.1016/j.margeo.2011.01.001>.
- Wang, Y., Zhu, D.K., 1990. Tidal flats of China. *Quat. Sci.* 4, 291–300.
- Wang, Y.G., Zhang, W.N., Huang, H.M., Chen, C., 2015. Review of studies on sources and transport of sediment in radial sand ridges. *Adv. Sci. Technol. Water Resour.* 35, 59–67 + 88.
- Wang, Z.B., 1992. Theoretical analysis on depth-integrated modelling of suspended sediment transport. *J. Hydraul. Res.* 30, 403–421. <https://doi.org/10.1080/00221689209498927>.
- Wang, Z.B., 1989. *Mathematical Modelling of Morphological Processes in Estuaries (PhD Thesis)*. TU Delft, Delft.
- Wang, Z.B., Louters, T., De Vriend, H.J., 1995. Morphodynamic modelling for a tidal inlet in the Wadden Sea. *Mar. Geol.* 126, 289–300.
- Wang, Z.B., Ribberink, J.S., 1986. The validity of a depth-integrated model for suspended sediment transport. *J. Hydraul. Res.* 24, 53–67. <https://doi.org/10.1080/00221688609499332>.
- Winterwerp, J.C., Lely, M., He, Q., 2009. Sediment-induced buoyancy destruction and drag reduction in estuaries. *Ocean Dynam.* 59, 781–791. <https://doi.org/10.1007/s10236-009-0237-y>.
- Winterwerp, J.C., van Kesteren, W.G., 2004. *Introduction to the Physics of Cohesive Sediment in the Marine Environment*. Elsevier Science Limited.
- Wu, W., 2004. Depth-averaged two-dimensional numerical modeling of unsteady flow and nonuniform sediment transport in open channels. *J. Hydraul. Eng.*
- Xing, F., Wang, Y.P., Gao, J.H., Zou, X.Q., 2010. Seasonal distribution of the concentrations of suspended sediment along Jianguo coastal sea. *Oceanol. Limnol. Sinica* 41, 459–468.
- Xing, F., Wang, Y.P., Wang, H.V., 2012. Tidal hydrodynamics and fine-grained sediment transport on the radial sand ridge system in the southern Yellow Sea. *Mar. Geol.* 291–294, 192–210. <https://doi.org/10.1016/j.margeo.2011.06.006>.
- Xu, F., Tao, J., Zhou, Z., Coco, G., Zhang, C., 2016. Mechanisms underlying the regional morphological differences between the northern and southern radial sand ridges along the Jianguo Coast, China. *Mar. Geol.* 371, 1–17. <https://doi.org/10.1016/j.margeo.2015.10.019>.
- Yao, P., Su, M., Wang, Z.B., van Rijn, L.C., Zhang, C.K., Chen, Y.P., Stive, M.J.F., 2015. Experiment inspired numerical modeling of sediment concentration over sand–silt mixtures. *Coast Eng.* 105, 75–89. <https://doi.org/10.1016/j.coastaleng.2015.07.008>.
- Zhang, C., Yang, Y., Tao, J., Chen, Y., Yao, P., Su, M., 2013. Suspended sediment fluxes in the radial sand ridge field of South Yellow Sea. *J. Coast Res.* 624–629. <https://doi.org/10.1016/j.coastaleng.2013.07.001>.

- [org/10.2112/SI65-106](https://doi.org/10.2112/SI65-106).
- Zhang, C., Zhang, D., Zhang, J., Wang, Z., 1999. Tidal current-induced formation - storm-induced change - tidal current-induced recovery. *Sci. China, Ser. A D* 42, 1–12. <https://doi.org/10.1007/BF02878492>.
- Zhang, C.K. (Ed.), 2012. *The Comprehensive Survey and Evaluation Report on Coastal Zone of Jiangsu Province*. Science Press, Beijing.
- Zhang, L., 2016. *The Coastal Erosion-deposition Evolution and Controlling Factors of the Abandoned Yellow River Delta in the Northern Jiangsu Province* (PhD Thesis). East China Normal University, Shanghai, China.
- Zhao, C.J., 2003. *Study on Power Sand Movement Laws in Coastal Dynamic Condition* (PhD Thesis). Tianjin University, Tianjin.
- Zhou, L., Liu, J., Saito, Y., Zhang, Z., Chu, H., Hu, G., 2014. Coastal erosion as a major sediment supplier to continental shelves: example from the abandoned Old Huanghe (Yellow River) delta. *Contin. Shelf Res.* 82, 43–59. <https://doi.org/10.1016/j.csr.2014.03.015>.